Geological Quarterly, 2025, 69, 61
DOI: https://doi.org/10.7306/gq.1834

Applicability of ICP-MS/AES, γ-ray and portable X-ray spectrometry (pXRF) data for rock-generated radiogenic heat calculations

Piotr SŁOMSKI[1, *] and Łukasz JASIŃSKI[1]

[1] Polish Geological Institute – National Research Institute, Lower Silesian Branch, al. Jaworowa 19, 53-122 Wrocław, Poland; ORCID: 0000-0003-1962-4449 [P.S.], 0000-0001-8385-392X [Ł.S]

Słomski, P., Jasiński, Ł., 2025. Applicability of ICP-MS/AES, γ-ray and portable X-ray spectrometry (pXRF) data for rock-generated radiogenic heat calculations. Geological Quarterly, **69**, 61; https://doi.org/10.7306/gq.1834

Associate Editor: Stanisław Z. Mikulski

Rock-generated radiogenic heat is one of the key parameters in assessing geothermal potential. To calculate it accurately, it is necessary to know the K, U and Th contents of the rocks in a given region. We have compared measurements of these element concentrations using results obtained by three analytical methods: γ-ray spectrometry, pXRF spectrometry and ICP-MS/AES. The measurements were made on the same samples. By employing statistical methods used in analytical and clinical chemistry, it was quantitatively demonstrated that pXRF tends to overestimate, and γ-ray spectrometry may underestimate (though to a lesser extent), the concentrations of U and Th by comparison with ICP-MS/AES. The scale of over- and underestimation is the especially large for samples with low contents of these elements. These discrepancies, especially in the case of pXRF measurements, lead to significant differences in the calculated radiogenic heat results, which can be many times higher (by up to two orders of magnitude) than those calculated on the basis of instrumental chemistry analyses. It can be concluded that both γ-ray spectrometry and pXRF spectrometry may be used for analyses to determine radiogenic heat. However, while the former method may be a primary research technique for this task (replacing instrumental chemical techniques), the latter should be used more as a screening technique, and may require calibration based on local standard samples obtained from the study area.

Key words: radiogenic heat, laboratory measurements comparison, statistical analysis.

INTRODUCTION

The presence and decay of the radioactive isotopes of potassium (^{40}K), uranium (^{238}U and ^{235}U) and thorium (^{232}Th) has a predominant influence on the amount of the radiogenic heat generated by rocks, which is an important factor in assessing geothermal potential (Rybach, 1988; Beardsmore and Cull, 2001; Mareschal and Jaupart, 2013; Hasterok and Webb, 2017). Therefore, measurements of potassium, uranium and thorium concentration in rocks are among the most common analyses performed during the evaluation of the geothermal potential of a certain region or geological unit (Zhang et al., 2024; Rafiq et al., 2025). The radiogenic heat generated has an especially significant impact on the thermal regime of the Earth's crust (Birch et al., 1968; Roy et al., 1968; Lachenbruch, 1970). Thermal effects related to the radiogenic heat generated may be visible at a local scale, e.g. in the surroundings of granites with a high content of radiogenic elements, the so called hot granites (Sliaupa et al., 2005). Secondary processes, such as hydrothermal alteration, physical and chemical weathering, or transport of eroded material, can lead to mixing and homogenization or further chemical differentiation (Fall et al., 2020), which may have impact of on the spatial and vertical distribution of radiogenic heat.

In Poland, elevated concentrations of K, U, and Th are found in the some regions of the Sudetes Mountains, the Carpathian Mountains, and the Holy Cross Mountains, as well as in the northeastern part of the country (Strzelecki et al., 1994). The Sudetes Mountains and their foreland have been the primary area of radiometric prospection in Poland, with studies and surveys conducted mainly between 1948 and the late 1980s (Lis et al., 1997; Solecki et al., 2011; Strzelecki and Wołkowicz, 2019). This region is particularly interesting due to its complicated geological structure and the diversity of rocks existing within it. The Sudetes and Fore-Sudetic Block consist of pre-Permian geological units that belong to the Variscan internides. These units are partially covered by syn- to post-orogenic Variscan and post-Variscan basins, which are filled with sedimentary and volcanic rocks (Mazur et al., 2025).

Lately, between 2021 and 2026, the Polish Geological Institute – National Research Institute (PGI-NRI), which fulfils the

* Corresponding author, e-mail: pslo@pgi.gov.pl

Received: September 20, 2025; accepted: December 15, 2025; first published online: January 12, 2026

tasks of the Polish Geological Survey, is managing a large geothermal project titled "Geothermal Atlas of the Sudetes and their Foreland". As a part of this project, an extensive campaign of sample collection has been carried out, both from surface exposures and from drilled cores. These samples were subjected to numerous laboratory analyses. Over 1700 samples were analysed for K, U and Th concentrations using the γ-ray spectrometry method. For quality control a subset of 98 unique samples, representing different lithologies, was also studied for its chemical composition using the inductively coupled plasma mass spectrometry/atomic emission spectrometry method (ICP-MS/AES). Furthermore, the same subset of 98 samples was analysed with a portable X-ray fluorescence spectrometer (pXRF), for methodological cross-checking.

In this research, we performed a statistical comparison of the results of K, U and Th concentrations obtained by these three analytical techniques. Our aim was to compare the agreement between the results provided by each of these analytical methods and to evaluate the applicability of these methods in providing suitable data for radiogenic heat calculations. By using samples representing various lithologies from the Sudetes area, our results can be applied to studies of K, U and Th contents in other regions of diverse lithology.

MATERIALS AND METHODS

SAMPLES AND ANALYTICAL TECHNIQUES

The samples were collected extensively in the years 2022 and 2023 across the Sudetes Mountains and the Fore-Sudetic Block in the SW part of Poland (Fig. 1). However, due to the differences in terrain relief, the highest density of sampling points was possible in the mountainous regions, where numerous rocky exposures are present. Over 1700 samples were analysed by means of γ-ray spectrometry, while 98 samples (Fig. 1) from this set were chosen to be studied in detail also by other instrumental techniques: ICP-MS/AES and pXRF. The samples chosen represent different geological units and lithologies. Acid igneous rocks are represented mainly by granites and granitic gneisses from the Izera-Karkonosze Massif, granites from the Strzegom-Sobótka Pluton, and granites and granitoids from the Kłodzko-Złoty Stok Pluton and the Kudowa Granite Pluton. Light-coloured metamorphic rocks include gneisses from the Góry Sowie Gneiss Massif, the Izera-Karkonosze Massif and the Orlica-Śnieżnik Dome, as well as metamorphic schists from the Strzelin Gneiss-Granite Massif and the Kaczawa fold belt. Dark-coloured metamorphic rocks such as amphibolites from the Kłodzko Metamorphic Massif and, to a minor extent, greenstones from the Kaczawa fold belt as well as serpentinites from the Ślęża Massif were also chosen for this study. The sample set is completed by sedimentary rocks, mainly sandstones and conglomerates, from the Intra-Sudetic Synclinorium. Additionally, one sample of basalt from the Izera-Karkonosze Massif was added, as representation of the basic igneous rocks. Due to the varied lithology of the samples and consequently also of their mineral composition, the range of K, U and Th concentrations was wide enough for a comprehensive comparative study. More detailed information about the samples is provided in Appendix 1.

The results of K, U and Th concentrations were compared, with measurements obtained using three independent instrumental techniques, each based on different physicochemical principles:

- γ-ray spectrometry,
- inductively coupled plasma mass spectrometry/atomic emission spectrometry (ICP-MS/AES);
- use of a portable X-ray fluorescence spectrometer (pXRF).

The γ-ray spectrometry measurements were conducted at the Petrophysical Laboratory of the Computational Geology Laboratory (PL-CGL) located at the Lower Silesian Branch of the PGI-NRI in Wrocław, Poland. Approximately 1 kg of each sample was crushed to a fraction smaller than 5 mm and carefully homogenized (quartered and mixed). This prepared material was used to fill a 585 ml cylindrical container (~700–800 g of material), which was tightly sealed. Measurements were performed after a waiting period of at least 14 days to allow for the establishment of equilibrium within the radioactive decay chains (Kalita et al., 1996). The analysis was conducted using a *GT-40 scintillation* gamma spectrometer (Moskalewicz, 2022; Kozlovska et al., 2023; Aghdam et al., 2024) equipped with a bismuth germanate detector (BGO, $Bi_4Ge_3O_{12}$). For the measurement, the sample was placed directly on the top of the spectrometer's detector. The detector itself is housed within a 10 cm thick lead shielding system, which effectively isolates it from ambient background radiation. The γ-ray spectrometry enables measurements in terms of uranium and thorium equivalents, eU and eTh, on the basis of their daughter products including ^{214}Bi and ^{208}Tl (Foote and Frick, 2001; McCay et al., 2014). Nevertheless, throughout this study, K_gamma, U_gamma and Th_gamma nomenclature will be used for distinguishing results obtained by this method. For the 98 samples chosen, the remaining crushed material was analysed by the two other techniques used in this study. We note that the material used for the ICP-MS and pXRF tests came from the same crushed and homogenized samples used for the γ-ray spectrometry measurements.

For the ICP-MS/AES analyses, the samples were sent to the ALS Global laboratory. The previously crushed material (fraction <5 mm) was delivered to ALS, where it was pulverized. Before analysis, the samples underwent various preparation procedures, including lithium borate fusion, followed by acid dissolution, aqua regia digestion, and four acid digestions. The detection limit for K_2O is 0.01%, and for U and Th it is 0.05 ppm. The measurement uncertainty information was provided by ALS with the results. The concentrations of the main elements were reported as weight percentages of oxides; however, the K_2O concentration was recalculated to pure potassium by multiplying K_2O concentration by a factor of 0.83 (this is the mass ratio of potassium in potassium oxide) and is denoted as K_chem. Similarly, U_chem and Th_chem refer to uranium and thorium concentrations (in ppm) from the ICP-MS/AES analyses.

The remaining powdered material from ALS Global was returned to the PL-CGL for the pXRF analyses. The measurements were made in XRF-dedicated cups, into which ~10 g of powdered sample was packed and covered with Mylar® foil. The instrument used for this study was an *Olympus Delta Premium pXRF* with a 50 kV X-ray tube. All measurements were performed in 3 Beam-Soil mode, with a long sample exposure time of 60 s per beam and 180 s for the total measurement time per sample, which is considered sufficient for obtaining the required accuracy (Zhou et al., 2023). To ensure better performance and accuracy, the measurements were repeated three times (total duration of 9 minutes per sample) and the results were averaged. Consequently, K_xrf, U_xrf and Th_xrf nomenclature will be used to distinguish the results obtained by this portable XRF spectrometer.

For radiogenic heat calculations, density values obtained in the PL-CGL were used in addition to the chemical data. The measurements of density and porosity were made according to

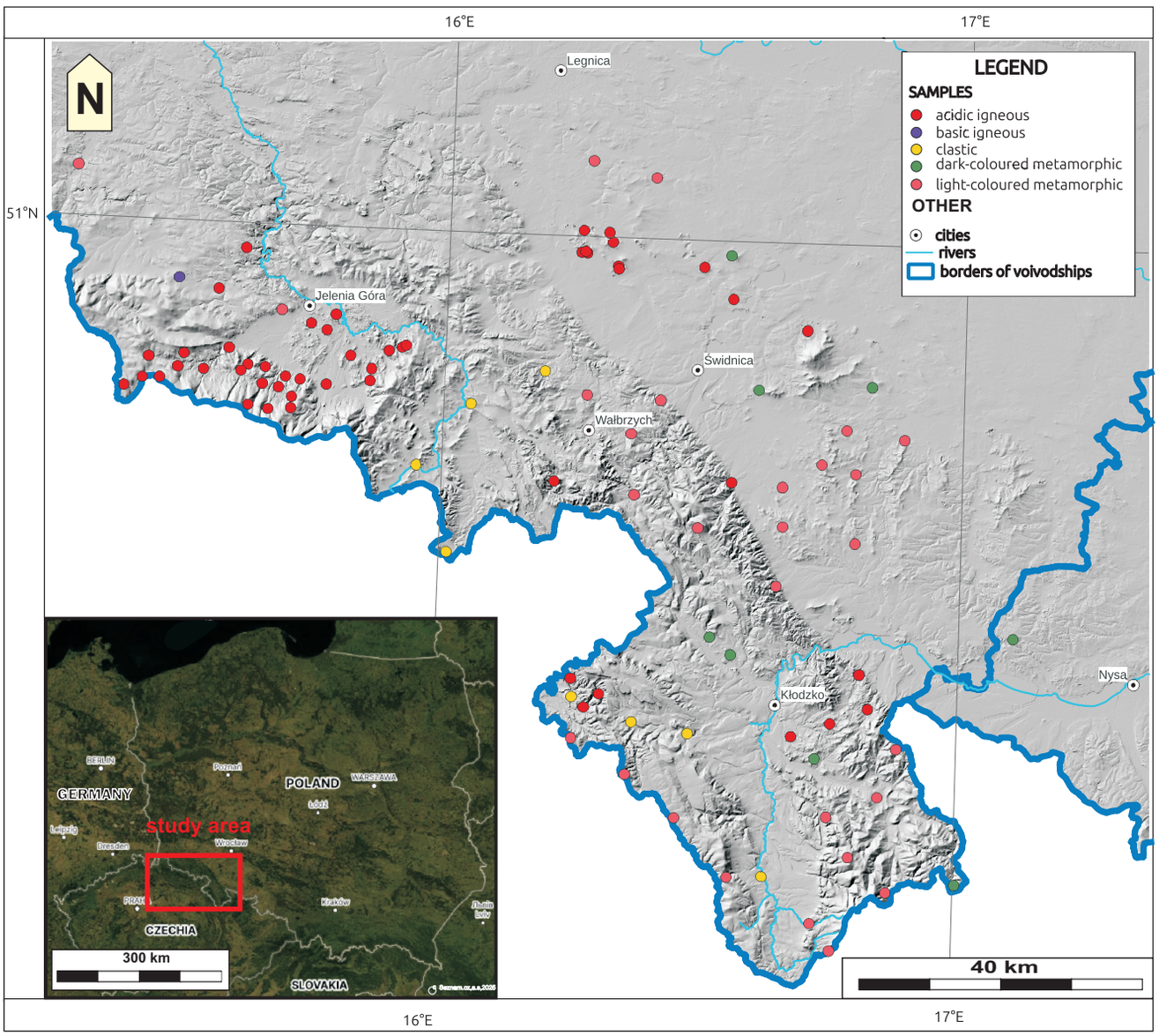

Fig. 1. Location of the study area (inset) and spatial distribution of igneous, metamorphic and sedimentary rock samples collected and chosen for laboratory comparative study

the water immersion porosimetry (WIP) methodology described by Kuila et al. (2014), with a minor modification to enable testing samples larger than 5 cm^3.

Knowledge of the concentrations of K (C_K), U (C_U) and Th (C_{Th}) in the rock, together with the density data (ρ), enables the calculation of rock-generated radiogenic heat (A). This is done according to equation [1] provided by Rybach (1988), with a modification from Sanjurjo-Sánchez et al. (2022) to use concentration as (K) instead of K_2O.

$$A \quad (9.67\ C_U \quad 2.56\ C_{Th} \quad 3.48\ C_K)\ 10^{-5}\ \frac{W}{m^3} \qquad [1]$$

STATISTICAL METHODOLOGY

When comparing measurements of the same quantitative variable, a strong correlation between the results obtained by two dedicated analytical methods should be expected, especially when the range of values is wide enough (Giavarina, 2015). However, a high value of correlation coefficient r or determination coefficient r^2 does not necessarily imply good agreement between the techniques compared. As demonstrated by Anscombe's quartet (Anscombe, 1973), different datasets (each containing paired observations X and Y) can share the same descriptive statistics and linear regression lines yet display completely different distributions when plotted on a cross-plot, therefore graphical visualisation is crucial.

Moreover, the well-known and widely used ordinary least squares (OLS) regression method is based on the assumption that values along the x-axis are error-free and that error minimization is performed only along the y-axis (James et al., 2023). By contrast, the comparison of results from two different techniques (or even from different apparatuses representing the same analytical technique) usually involves comparison of paired values from two datasets, both with their own measure-

ment uncertainties (Ludbrook, 2010; Giavarina, 2015). To address this issue, a regression method that accounts for uncertainties of each method (along the x and y axes), should be used.

In this work, in order to properly compare the results obtained by means of ICP-MS/AES with the results from γ-ray and pXRF spectrometry, we used two statistical methods commonly used in analytical and clinical chemistry: a robust regression method developed in the 1980s by Passing and Bablok (1983, 1984); Bablok et al. (1988) and Bland-Altman plots (Altman and Bland, 1983). More details about these two methods can be found in Appendix 2. All statistical operations and calculations, as well as data visualisation, were performed with the use of R programming language (The R Core Team, 2025), including packages *ggplot2* (Wickham, 2016), *ChemoSpec* (Hanson, 2025) and *mcr* (Potapov et al., 2012).

RESULTS

EXPLORATORY DATA ANALYSIS

In this section, the concentrations of K, U and Th are given with a clear distinction for each technique used. The data are plotted on a set of boxplots, histograms and quantile plots, shown in to 4. Detailed statistical information is gathered in Table 1, while the complete results are available in Appendix 1.

The ranges of K_chem and K_gamma values are nearly identical, from 0.02 to ~5.37 wt.%, while the median values are both ~3.5 wt.% (Fig. 2A). The pXRF method (K_xrf results) provided data within a range of 0 to 5.09 wt.% and a slightly lower median of 3.16 wt.% (Fig. 2A). The datasets of K_chem and K_gamma results also have a similar 1st quartile (~2.4 wt.%), while K_xrf data are characterized by a slightly lower value, 2.24 wt.%. For the 3rd quartile, the values are 3.93 and 3.81 wt.% for K_chem and K_gamma data, respectively, but the K_xrf data value is only 3.4 wt.%. For comparison, the average concentration of potassium in the upper continental crust (UCC) is estimated at 2.87 wt.% (Wedepohl, 1995). In each set of laboratory results, the highest potassium concentration, usually above the 1st quartile, is observed for most of the acid igneous and light-coloured metamorphic rocks analysed (Fig. 2A). The lowest K content, <1 wt.%, was found in dark-coloured metamorphic rocks, some clastic rocks as well as in the basalt sample (Fig. 2A).

Despite their different ranges, the results from each of the techniques applied show a similar data distribution. A comparison of the quantile plots and histograms (Fig. 2B, C) clearly reveals that the distribution for K_chem, K_gamma and K_xrf all have a negative skewness, which in each case is ~–0.9 ±0.05 (Table 1).

For each measurement method, values more than one standard deviation below the mean were observed more frequently than in a normal distribution. However, for the K_chem and K_gamma results, values more than one standard deviation above the mean are less frequent than in a normal distribution (Fig. 2B, C). All the distributions of potassium concentration are mesokurtic and the kurtosis values are –0.05, 0.07 and 0.38 for K_chem, K_gamma and K_xrf, respectively (Table 1). The higher value of kurtosis for K_xrf is clearly visible on the histogram and distribution plot (Fig. 2C).

The range of uranium concentrations obtained from γ-ray spectrometry shows a remarkably similar pattern to the one representing the chemical data. Minimum values oscillate ~0, while the maximum values are ~20 ppm for both techniques (Fig. 3A). In contrast, portable XRF measurements indicate a higher range, varying from 2.5 to 26.7 ppm, with a median value of 6.2 ppm (Fig. 3A). The value of the 1st quartile for U_chem and U_gamma results is nearly identical and equal to ~1.9 ppm, whereas for the U_xrf it is significantly higher at ~4.42 ppm. The value of the 3rd quartile is lowest for the U_gamma data (4.2 ppm), while the U_chem results are characterized by a value of 5 ppm and U_xrf is even higher, at 9 ppm. Wedepohl (1995) gives 2.5 ppm as the average concentration of uranium in the UCC.

The highest concentration of uranium, usually between the 1st quartile and 10 ppm, were observed for samples of acid igneous and light-coloured metamorphic rocks (Fig. 3A) in the U_chem and U_gamma data sets. In all data sets, samples of sedimentary rocks show U values <1st quartile. Dark-coloured metamorphic rocks show almost no uranium content in the U_chem and U_gamma data sets; however, in case of the U_xrf data, the results for the dark-coloured metamorphic rocks and the basalt sample showed values between 6 and 9 ppm (1st quartile and median), while results for the acid igneous and light-coloured metamorphic rocks fall within the range of 5–15 ppm for most of the samples (Fig. 3A).

The distributions of uranium concentrations obtained by each analytical technique show a positive skewness (Fig. 3B, C). The skewness values are 2.29, 2.97 and 1.75 for U_chem, U_gamma and U_xrf, respectively (Table 1). The pattern observed on the quantile plots is similar for all methods. Values >1.5 standard deviations below the mean are less frequent than in a normal distribution. Conversely, values more than one standard deviation above the mean are observed more frequently than in a normal distribution (Fig. 3B), particularly for the U_chem and U_gamma data. All uranium concentrations are leptokurtic, with kurtosis values of 8.85, 15.49 and 5.98 for U_chem, U_gamma and U_xrf, respectively (Table 1). The differences in kurtosis are clearly visible on the histograms and distribution plots (Fig. 3C).

An analogous situation is observed for the thorium data. The minimum values from the Th_chem and Th_gamma data are both <0.1 ppm, while the maximum values exceed 40 ppm. The medians of these datasets are 12.3 and 13.47 ppm, respectively (Fig. 4A).

On the other hand, the results from the portable XRF fall in the range 2.67–61 ppm, with a median value of 35.4 ppm (Fig. 4). The 1st quartile of the Th_chem and Th_gamma data has values of 8.37 and 8.68 ppm, respectively, whereas the same statistic for Th_xrf dataset is more than twice as large, reaching 18.3 ppm (Fig. 4 and Table 1). The 3rd quartiles for Th_chem and Th_gamma are also very similar, represented by values of 20.9 and 21.27 ppm, while the same quartile for the Th_xrf dataset is 35.4 ppm (Fig. 4 and Table 1). The average amount of thorium in the UCC is 10.3 ppm according to Wedepohl (1995).

Most of the igneous acid rock samples showed the highest thorium concentrations, above the median value from each set of Th measurements; light-coloured metamorphic rocks indicate values mainly between the 1st quartile and the median value of each set of Th results (Fig. 4A). Dark-coloured metamorphic rocks and sedimentary rocks show the lowest Th amounts, <8 ppm (Fig. 4A). The one basalt sample also had a Th concentration below 8 ppm in the Th_chem and Th_gamma data sets, but in Th_xrf results the Th amount in that sample showed almost 50 ppm.

The distributions of the thorium concentrations from each analytical technique show a slight positive skewness (Fig. 4B, C), with skewness values ranging from 0.3 to 0.53 (Table 1). Only a few data points representing the lowest concentrations,

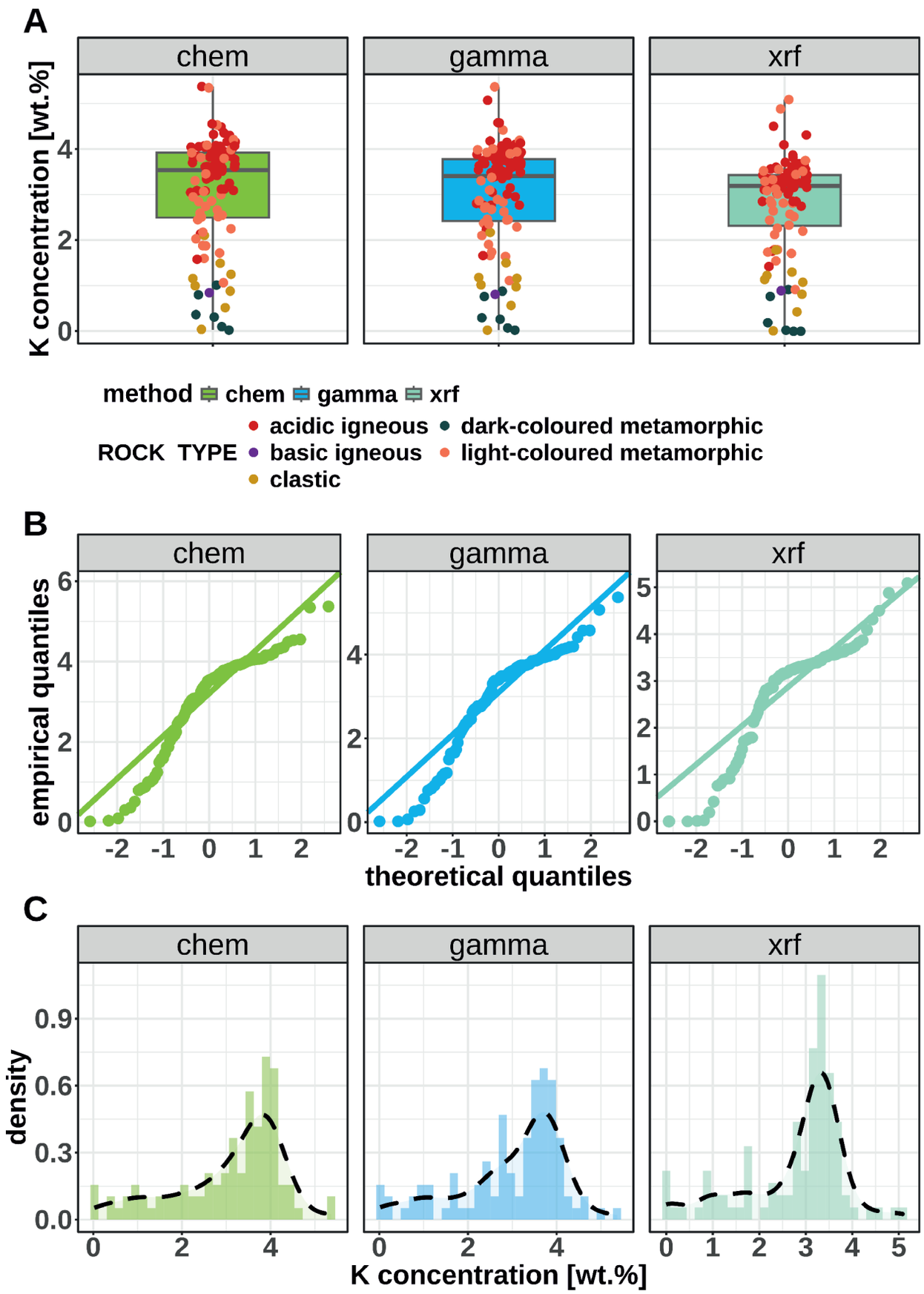

Fig. 2. Distributions of potassium concentration obtained by means of ICP-MS/AES, gamma spectrometry and pXRF spectrometry

A – boxplots, whereas boxes represent the first (lower edge) and third quartiles (upper edge) of the data, while the bar inside the box indicates the median value; **B** – quantile plots, where the solid line indicates the norm distribution patterns; for points below the mean (located along the negative section of the x-axis), being below the solid line indicates a higher frequency than expected from the normal distribution, while being above the line indicates a lower frequency; for points above the mean (located along the positive section of the x-axis), the opposite rule applies; **C** – histograms and simplified distribution curves

Table 1

Statistical parameters of measurements of K, U and Th concentrations

Element	Method	MIN	p25	M	MED	p75	MAX	SD	MAD	SK	K
K	chem	0.02	2.4	3.06	3.54	3.94	5.37	1.24	0.79	–0.87	–0.05
K	gamma	0.02	2.36	2.98	3.4	3.81	5.37	1.2	0.85	–0.87	0.07
K	xrf	0.00	2.25	2.77	3.16	3.43	5.09	1.11	0.59	–0.95	0.38
U	chem	0.03	1.96	4.00	3.40	5.05	20.70	3.10	2.29	2.29	8.85
U	gamma	0.00	1.86	3.35	2.97	4.16	19.59	2.61	1.72	2.97	15.49
U	xrf	2.50	4.42	7.04	6.20	9.00	26.67	3.82	3.43	1.75	5.98
Th	chem	0.06	8.37	14.28	12.32	20.93	40.50	8.74	9.81	0.52	–0.07
Th	gamma	0.00	8.68	14.77	13.47	21.27	43.03	9.32	9.66	0.53	–0.07
Th	xrf	2.67	18.3	27.22	26.12	35.45	61.00	12.10	13.42	0.30	–0.21

MIN – minimum, p25 – 1st quartile, M – mean, MED – median, p75 – 3rd quartile, SD – standard deviation, MAD – median absolute deviation, SK – skewness, K– kurtosis

particularly from the Th_chem and Th_gamma datasets, deviate from a normal distribution by being less frequent (Fig. 4B, C and Table 1). The kurtosis of the thorium concentration distributions is within a narrow range, from –0.21 to –0.07 (Table 1).

All three sets of measurements have similar statistical characteristics, as detailed above. Since all samples used for each analytical technique were from the same source and were perfectly homogenized. Therefore, the differences observed in the ranges and specific details of the distributions among these results stem from the performance of each method and its ability to accurately measure varying concentrations of K, U and Th in complex geological samples.

The characteristics of the sample density (bulk density) data are shown in Figure 5. The set of samples studied shows a broad range of densities, from ~2.3 to almost 3 g/cm^3 (Fig. 5A). However, most samples fall in the range ~2.5 and 2.65 g/cm^3 (corresponding to the 1st and 3rd quartiles of the data, respectively).

The density data distribution is close to a normal distribution, but with so-called “heavier tails”, which means that both the lowest and highest values are more likely to appear (Fig. 5). The distribution also has a slightly positive skewness (value 0.86), while the value of kurtosis is 4.9 (leptokurtic distribution). The wide range of density values is a consequence of the diverse lithologies of the sample suite and falls within the typical rock density values of 2–3.5 g/cm^3 given by Schön (2015).

COMPARATIVE ANALYSIS

REGRESSION

An analysis was made of cross-correlations between measurements obtained by γ-ray spectrometry and portable XRF spectrometry with instrumental chemistry results (Fig. 6). The values of the Pearson *r* correlation coefficient, slopes and y-interception coefficients obtained by means of Passing-Bablock regression are discussed in the text, while ordinary least squares slopes and y-interception coefficients are shown on the plots for comparison.

The comparison between K_chem and K_gamma data indicates a nearly perfect agreement between the gamma spectrometry and instrumental chemical analysis results (Fig. 6A). The fitted regression line slope is very close to 1 (0.96), the y-interception coefficient is 0.02, and the *r* coefficient is 0.99.

A correlation between the K_chem and K_xrf results is also clearly visible, however, most results deviate from the y = x line, as the K_xrf results are consistently lower than the K_chem results (Fig. 6B). The slope is 0.86 and the y-intercept is 0.10, while *r* is 0.98. The r coefficient is nearly identical for both comparisons, despite the differences in slopes and y-intercepts. This demonstrates that simple OLS regression may not be an appropriate method for evaluating the relationship between these two independent laboratory methods.

Figures 6C and D compare uranium concentrations between the U_chem and U_gamma datasets, and the U_chem and U_xrf datasets, respectively. The U_gamma results tend to be underestimated relative to the U_chem data, especially for samples containing more than ~6 ppm. Nevertheless the agreement between the results is good, with the fitted regression line having a slope of 0.82, a y-intercept of 0.06 and *r* of 0.96 (Fig. 6C).

The agreement between U_chem and U_xrf is at most of average quality. The pXRF method overestimates uranium concentration, and the data points are clustered rather than showing a clear linear relationship, resulting in an *r* of only 0.79 (Fig. 6D). The fitted regression equation has a slope of 1.32 and a y-interception coefficient of 1.17. Please note that the equation fitted from the OLS method has a slope of 0.97 and a y-interception coefficient of 3.15, which is very different from the Passing-Bablock regression and may falsely suggest better agreement between the methods.

Similarly to the potassium measurements, the thorium results from chemical analysis (Th_chem) and gamma spectrometry (Th_gamma) show a nearly perfect correlation (Fig. 6E). The slope of the fitted regression line is 1.05, the y-intercept coefficient is –0.33 and *r* is 0.99.

On the other hand, the thorium concentrations obtained using the pXRF instrument indicate systematic overestimation when compared with the Th_chem results (Fig. 6F). Although,

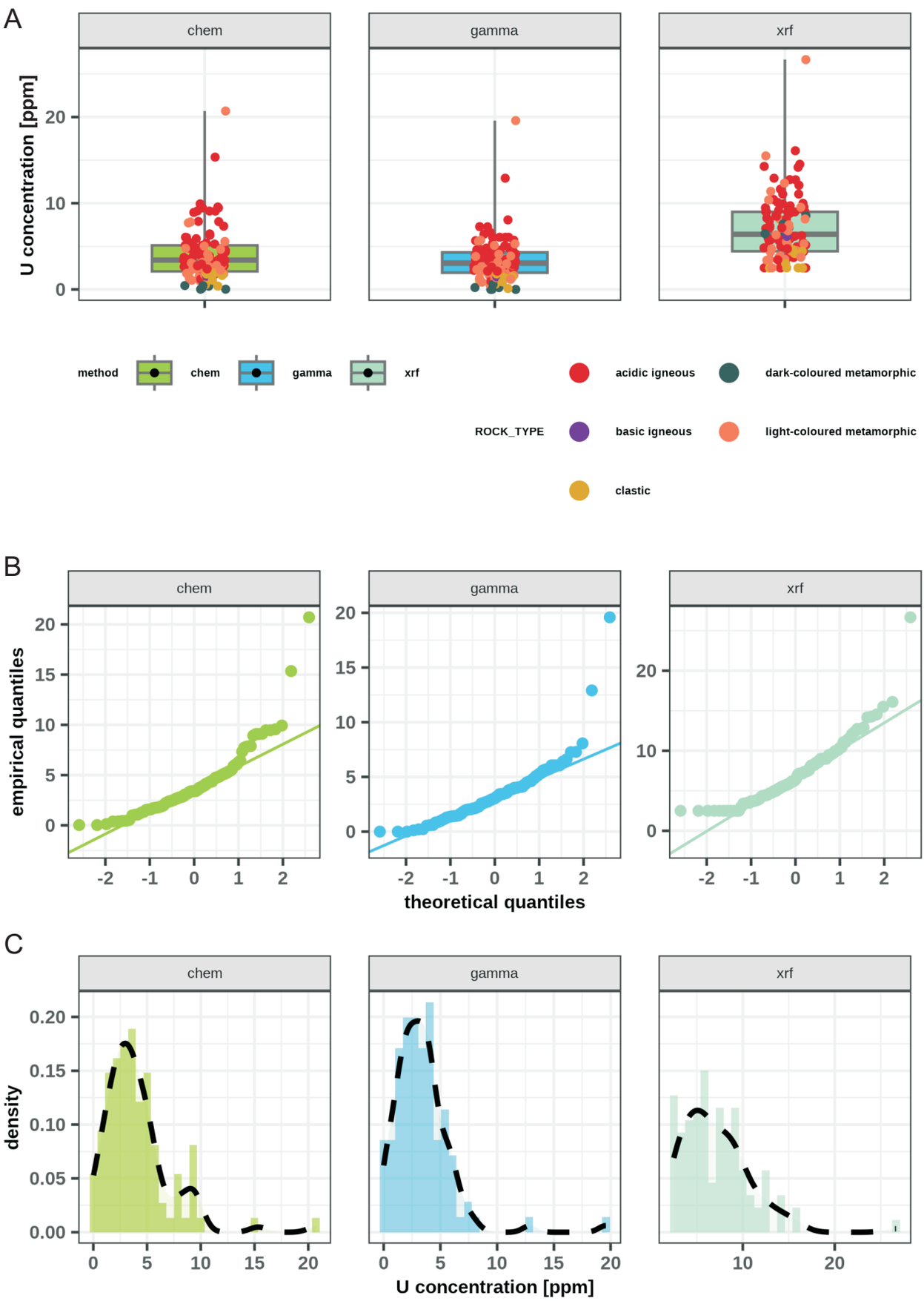

Fig. 3. Distribution of uranium concentrations obtained by means of ICP-MS/AES, gamma spectrometry and pXRF spectrometry, shown on: A – boxplots, B – quantile plots, C – histograms and simplified distribution curves

For explanations see Figure 2

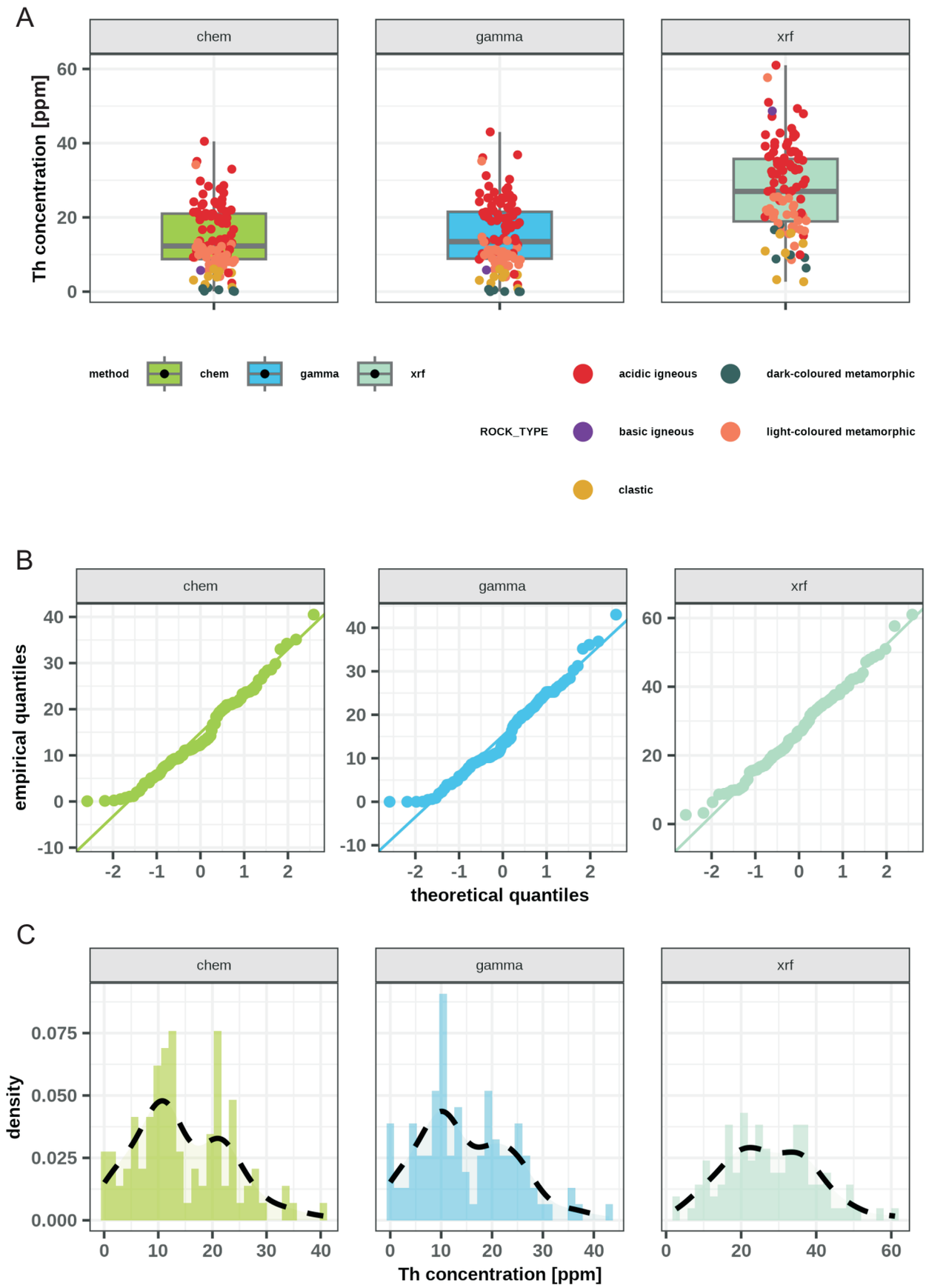

Fig. 4. Distribution of thorium concentrations obtained by means of ICP-MS/AES, gamma spectrometry and pXRF spectrometry, shown on: A – boxplots, B – quantile plots, C – histograms and simplified distribution curves

For explanations see Figure 2

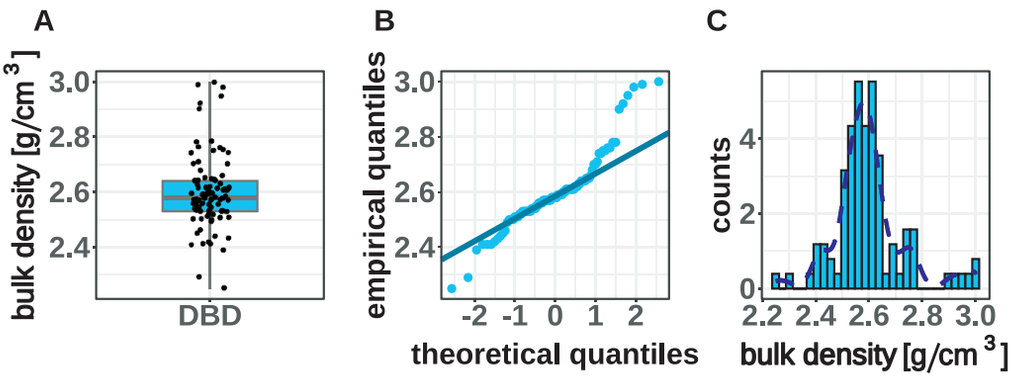

Fig. 5. Distribution of bulk densities of the samples analysed, shown on: A – boxplot, B – quantile plot C – histogram with simplified distribution curve

For explanations see Figure 2

these results are arranged mostly in a linear pattern and a correlation coefficient is high (0.92), which indicates strong correlation, nevertheless the Passing-Bablock slope value equals 1.38 and the y-intercept is 6.99.

BLAND – ALTMAN PLOTS

Analysis of the Bland-Altman plots (Figs. 7–9) allows for a detailed investigation of the differences between the results obtained using the analytical methods compared.

With the potassium results, a comparison of K_gamma vs. K_chem data (Fig. 7A) and K_xrf vs. K_chem data (Fig. 7B) reveals a similar trend: the largest relative differences are seen in samples with low potassium contents (a mean value of <~1 wt.%). For most samples with higher concentrations, the relative difference decreases rapidly and stabilizes around its mean value. The greatest relative difference between the K_gamma and K_chem reaches up to –60%, but for most samples, it is within the range of ±10% (Fig. 7A). For the K_xrf and K_chem results, the greatest relative difference is significantly higher, reaching up to –200%. However, for most of the samples it is within the range of ±20% (Fig. 7B). In both comparisons, the plots indicate that the difference between the methods is concentration-dependent, being larger for low concentration measurements and approaching a constant level for higher concentrations.

A Bland-Altman plot visualizing the measurements of U_gamma and U_chem (Fig. 8A) reveals that the highest relative differences (up to –200%) are observed for samples with very low uranium concentrations (mean of methods <1 ppm). In this case, the relative difference between the methods does not decrease with increase of the mean value of the results from both methods. For measurements representing higher concentrations (mean of methods up to 10 ppm), there are samples with a near-zero difference between the results from both methods. Nevertheless, many samples in this range show a relative difference of from ~25 to –50% (Fig. 8A).

A lack of a clear pattern on the plot in B (especially for the mean of results up to ~10 ppm) shows that the differences between the U_chem and U_xrf do not decrease strongly with increasing concentration. The values of the relative differences between U_chem and U_xrf range from 210 to –60%. Two samples representing the highest concentrations of uranium are characterized by a relatively low relative difference in values (<±30%), in both the U_chem vs. U_gamma and U_chem vs. U_xrf comparisons (Fig. 8A, B).

The relationships between Th_chem and Th_gamma reveal the same pattern as for analogous measurements for potassium (Figs. 7A and 9A). The difference between the methods changes with concentration, from greater for measurements of low concentration, while approaching a constant level for higher ones. The greatest relative difference between Th_gamma and Th_chem results reaches up to –200%, but for most of the samples, it falls within the range of ±25% (Fig. 9A).

The same situation is observed for Th_xrf and Th_chem data. However, the relative difference between these methods is moderately large; even for samples with higher concentrations (>10 ppm) it ranges from ~75 to ~30% (Fig. 9B). Measurements made on samples containing ≤~10 ppm of thorium are characterized by relative difference values ranging from 200 to 70% (Fig. 9B).

The samples that showed the greatest differences in K, U, and Th concentrations represented mainly dark-coloured metamorphic rocks and, to a lesser extent, clastic sedimentary rocks. The best agreement between the methods was observed for acidic igneous rocks and light-coloured metamorphic rocks, which showed the highest contents of the elements analysed.

ROCKS-GENERATED RADIOGENIC HEAT

The results of the calculation, based on the data from each technique used in this study, are shown in Figure 10. According to Wollenberg and Smith (1987) rock-generated radiogenic heat in the upper continental crust may display a broad range of values from 0 for basic extrusive rocks up to 30–45 $\mu W \cdot m^{-3}$ for acid igneous and metamorphic rocks. Regardless of the analytical method used, the radiogenic heat calculated for our samples does not exceed 8 $\mu W \cdot m^{-3}$; however, most of the results exceed the average value of radiogenic heat generated in the upper continental crust, which is ~1.6 $\mu W \cdot m^{-3}$ (Jaupart et al., 2016).

It is clear that the A values based on pXRF (A_xrf) measurements are significantly higher than the values calculated using ICP-MS/AES (A_chem) and gamma spectrometry (A_gamma) data, which are broadly comparable. The range of A obtained

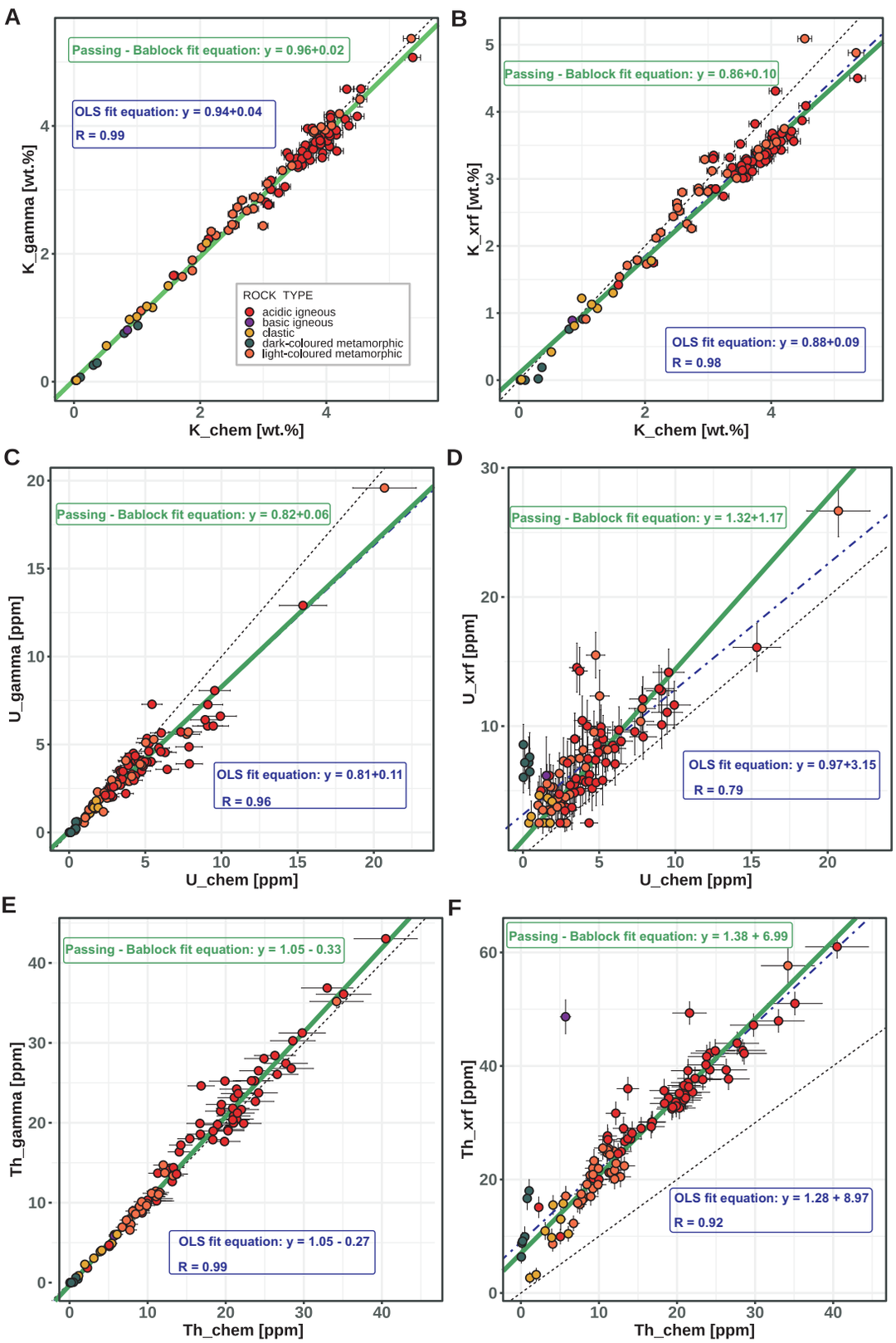

Fig. 6. Passing-Bablok regression plots of A – K_chem vs. K_gamma; B – K_chem vs. K_xrf; C – U_chem vs. U_gamma; D – U_chem vs. U_xrf; E – Th_chem vs. Th_gamma; F – Th_chem vs. Th_xrf

Regression equations both for Passing-Bablock and OLS regressions are given on the graphs

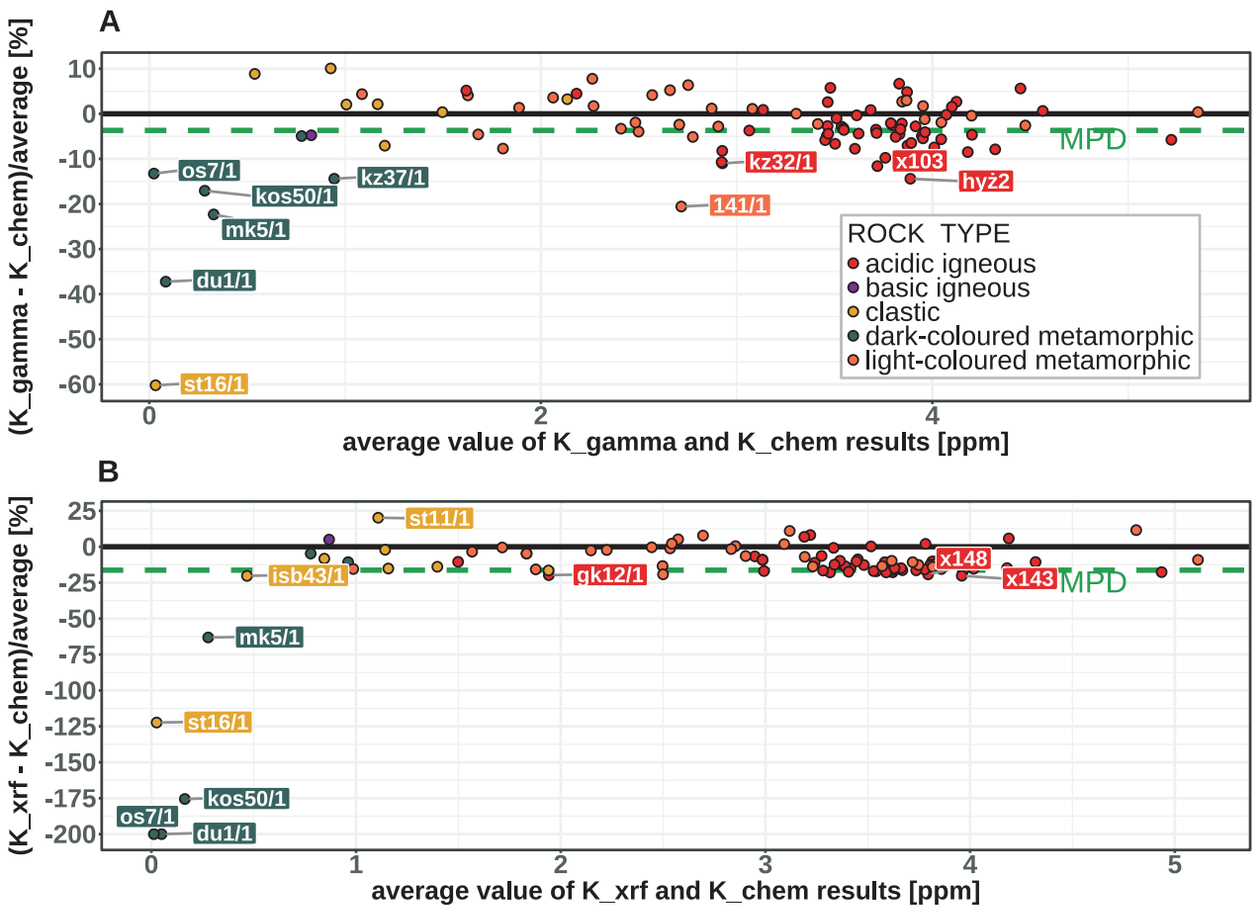

Fig. 7. Bland-Altman plots for A – K_gamma vs. K_chem and B – K_xrf vs. K_chem

from pXRF is between 0.75–8 μW · m^{-3}, while for the other two techniques, the calculated A values fall within the range of 0 to ~6 μW · m^{-3}.

Given the significant differences in the calculated radiogenic heat values for the samples selected, we have shown (Fig. 11) the A values based on pXRF and gamma spectrometry normalized (divided) by the A values calculated from chemical analysis.

For most samples, the A_gamma/A_chem ratio oscillates ~1, while the ratio of A_xrf/A_chem ranges from 1.5 to 3 (A); however, for samples with the lowest values of A, the A_xrf /A_chem ratio increases, ranging from 5 to 200 (Fig. 11A). The opposite trend is seen for the A_gamma /A_chem ratio, as it is <0.75 for some of these low-concentration samples (Fig. 11A).

Although the same pattern is plotted on panels B, C and D of Figure 11, the points are coloured according to the decimal logarithms of the ratios of K, U and Th contents from the pXRF and γ-ray spectrometry, respectively, to the concentrations of these elements obtained from instrumental chemistry (Fig. 11B–D). This approach allowed for a graphical presentation of the relevant ratios of individual analyses, which differ from each other by up to two orders of magnitude.

It is seen that while most of samples do not differ significantly in their potassium results, some samples with the highest A_xrf /A_chem ratio and lowest A_gamma /A_chem ratio are depleted in K according to the pXRF and γ-ray measurements, since the $\log_{10}$(K_xrf/K_chem) and $\log_{10}$(K_xrf/K_chem) ratios are <0 (Fig. 11B). Meanwhile, the same samples show an overestimation of uranium content in the pXRF results compared to U_chem, with highest $\log_{10}$(U_xrf/U_chem) ratios, ranging from 0.5 to 2.5, which corresponds to pXRF measurements being ~3 to 300 times higher than the chemical analyses. In contrast, an underestimation of uranium concentration in γ-ray spectrometry results compared to U_chem results is observed, since some samples indicate $\log_{10}$(U_gamma/U_chem) ratios, ranging from –0.2 to –0.5 (this corresponds to γ-ray measurements being approximately some 3 times lower than those from chemical analyses) or being undefined (for the samples indicating no U in γ-ray spectrometry measurements).

Exactly the same characteristics are observed for the $\log_{10}$(Th_xrf/Th_chem) ratio, which ranges from 0.5 to 2 (corresponding to pXRF measurements being ~3 to 100 times higher than those from chemical analyses) and for the $\log_{10}$ (U_gamma/Th_chem) ratio, which have values between –0.25 and –1 (corresponding to γ-ray measurements being approximately up 10 times lower than those from chemical analyses), or are undefined for the samples with no Th detected by spectrometry measurements (Fig. 11D).

The samples showing the greatest ratio of A_xrf and A_gamma to A_chem (>3; Fig. 10) are the same ones that show the greatest relative differences in the Bland-Altman plots (Figs. 7–9). These differences are especially great in the U and Th samples representing dark-coloured metamorphic rocks: os7/1, mk5/1, kz37/1, du1/1, mk2/1, kos/50/1, sedimentary rock samples st/16/1, st28/1, basalt sample iz39/1, and one granitoid sample gs89/1. Although, most of the samples show a rela-

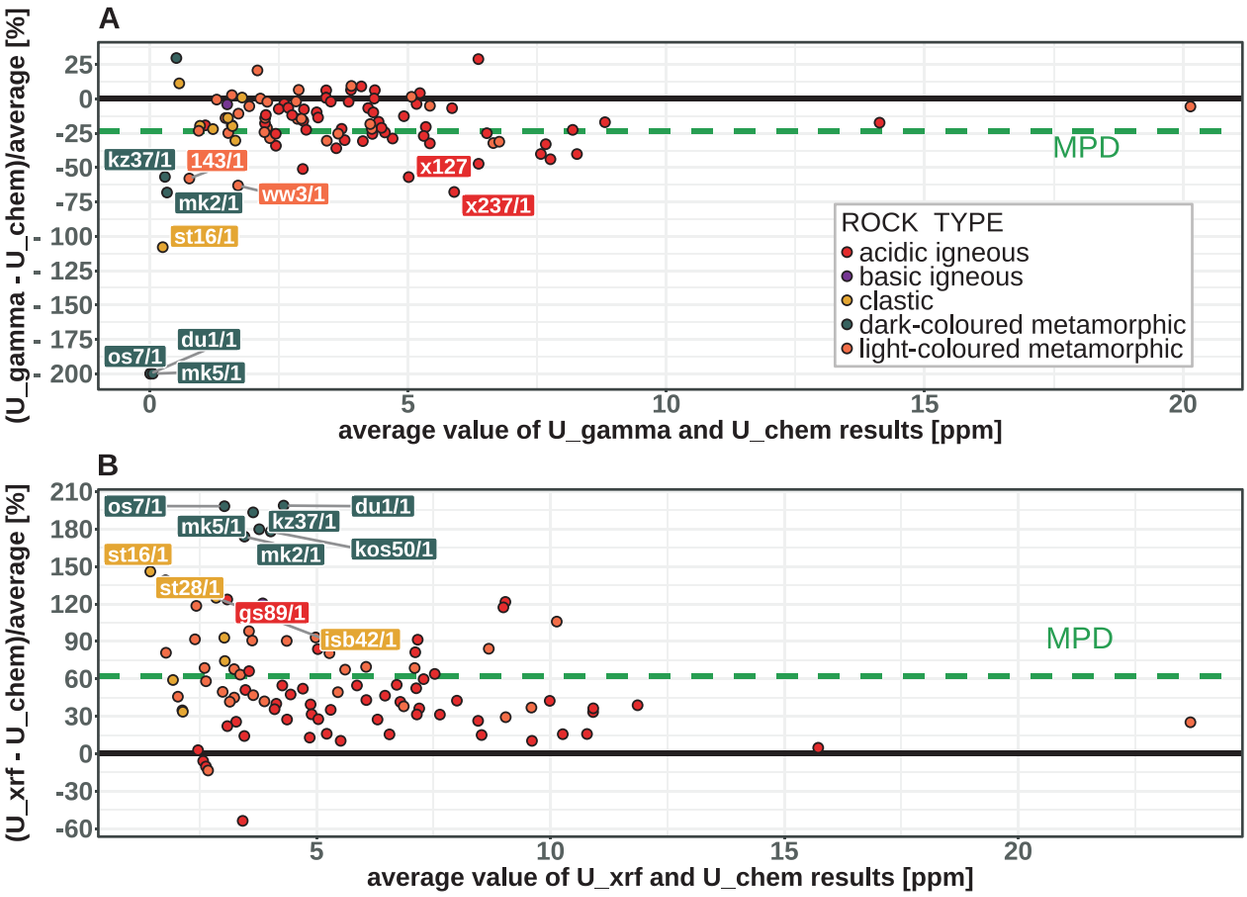

Fig. 8. Bland-Altman plots for A – U_gamma vs. U_chem and B – U_xrf vs. U_chem

tively lower absolute ratio of A_xrf and A_gamma to A_chem (from 1.5 to 3); they still indicate high radiogenic heat values in A_chem, so such overestimation will have significant consequences when estimating the geothermal potential of a given region. This applies to the γ-ray results for granite sample x159 as well as a series of pXRF measurements (Fig. 10 and Appendix 1). These specific samples are characterized by U_xrf and U_gamma as well as Th_xrf and Th_gamma concentrations 1.3 to 3 times higher than the corresponding chemical measurements (logarithmic ratios from 0.1 to 0.5 in Fig. 11C and D).

DISCUSSION

As shown in the Results sections, on the Figures 6C–F, 7–9 and 11B–D, the pXRF measurements tend to significantly overestimate the concentrations of U and Th for some samples. Conversely, gamma spectrometry slightly underestimate these concentrations in a small number of samples when compared to ICP-MS/AES data.

Some researchers argue that analysing low concentrations of U and Th can be challenging for ICP-MS/AES methods. Potential issues include incomplete element extraction during sample digestion, possible contamination during preparation, and spectral interferences (Tuovinen et al., 2015). However, many studies indicate that ICP-MS/AES can be considered a reference technique for analysing even low-detection concentrations of U and Th, especially when proper sample treatment is performed prior to analysis (i.e., Nisi et al., 2009; Steiner et al., 2017; Lemière, 2018; Zhou et al., 2023). Since a multi-acid digestion procedure was applied to our samples, we maintain that the ICP-MS/AES results can be treated as a reference for the other two methods. Furthermore, the fact that we analysed exactly the same powdered samples strengthens the robustness of our comparisons.

The greatest overestimation of U and Th values in our pXRF data is observed for samples containing <5 ppm of U and <10 ppm of Th (Figs. 6D, F, 8B and 9B). This is not surprising, as the detection limit for uranium and thorium for low-density samples is <5 ppm, according to the specifications of *Olympus Delta pXRF* and other publications (Durance et al., 2014).

Tuovinen (2015) reported good agreement between pXRF and ICP-MS measurements of U and Th, although these tests were performed on U and Th-rich ore samples. These samples generally indicate much higher values of U and Th, even exceeding the 3rd quartile value in our datasets. A comparison of pXRF for a wide range of U (0–35000 ppm) and Th (0–1000 ppm) concentrations by Knight et al. (2021) also showed good correlation between pXRF uranium results and reference values. However, he found that pXRF overestimated U concentration for samples with <40 ppm of U, which is consistent with our measurements.

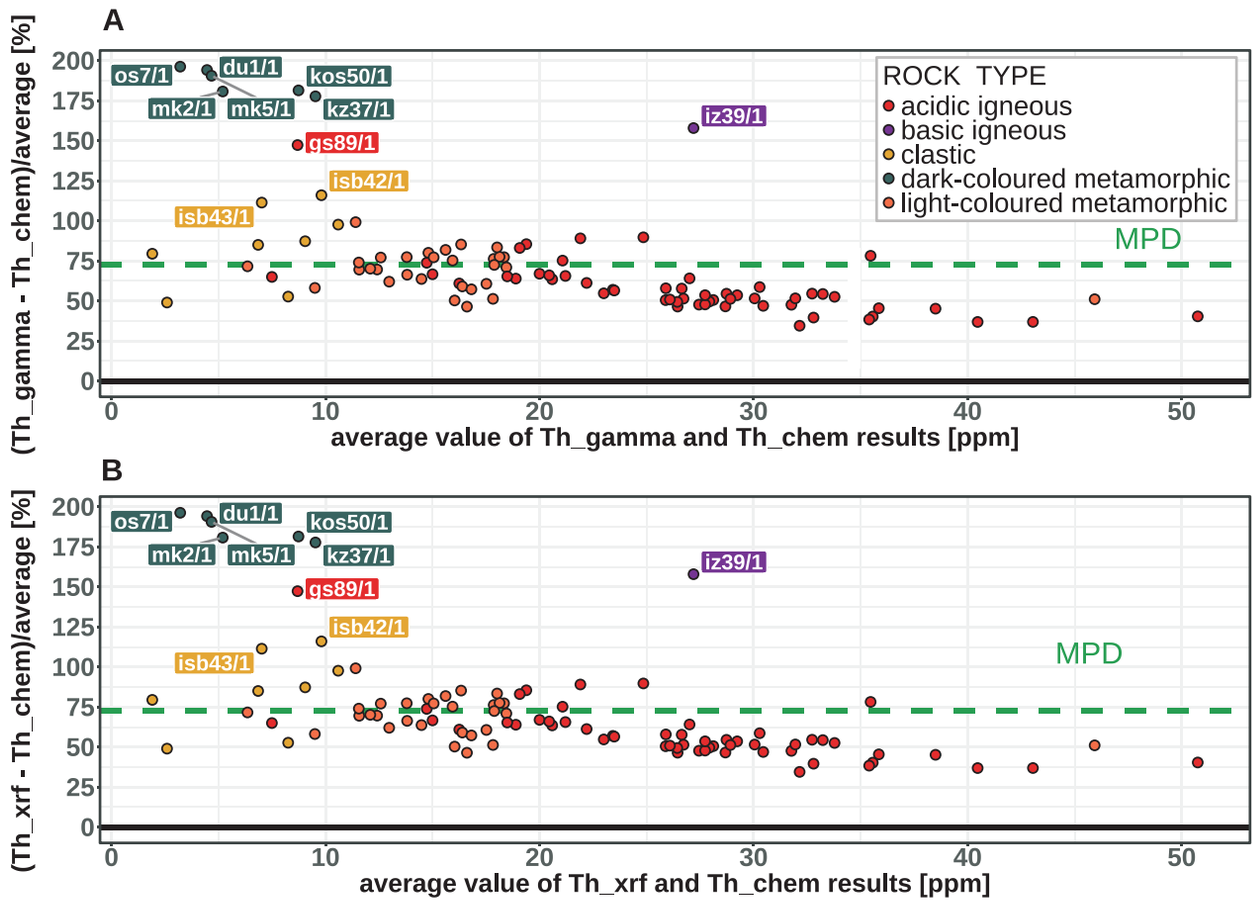

Fig. 9. Bland-Altman plots for A – Th_chem vs. Th_gamma and B – Th_chem vs. Th_xrf

The explanation for the overestimation of uranium and thorium content in the pXRF measurements of samples with relatively low concentrations lies in the chemical composition of the Standard Reference Material (SRM) used to calibrate this technique and in the matrix composition of the samples analysed. According to Melquiades (2024), if the Zr, Rb and Sr contents in the SRM and samples significantly exceeds the uranium and thorium concentrations, the K-lines from Rb, Sr, and Zr peaks may overlap the L-lines from Th and U peaks. This spectral interference causes an inter-element enhancement effect (Van Grieken and Markowicz, 2001) and falsely elevates the concentrations of U and Th in the pXRF results.

This description exactly fits also to our results, which is clearly visible in the spectra of our measurements, where significant K-lines from Rb, Sr, and Zr are visible (Fig. 12). The *Olympus Delta Premium pXRF* instrument used in this study has a factory calibration made by the Compton normalization method, using NIST 2710 and 2711 SRM (Olympus, 2010; US EPA, 2007). The concentrations of U and Th are respectively 25 and 12 ppm in NIST 2710, while NIST 2711 contains 2.6 and 14 ppm of U and Th. For comparison, the concentrations in NIST 2710 are 120 and 330 ppm, respectively for Rb and Sr, while this SRM does not contain Zr. NIST 2011 is contains 110 ppm of Rb, 245.3 ppm of Sr and 230 ppm of Zr. There is no doubt that concentrations of Rb, Sr and Zr are higher than those of U and Th, both in the SRMs and in the samples analysed by us, which may impact the quality of results.

The manufacturer of the SRMs, the National Institute of Standards and Technology informs that only the Sr content in NIST 2711 is a certified value, while the rest are noncertified values, which mean that a bias was suspected in one or more of the methods used for certification, or two independent methods were not available (NIST, 2005). Nevertheless Rb, Sr and Zr can be measured according to the *Olympus Delta pXRF* manufacturer (Olympus, 2010).

The underestimation of the amount of potassium (Figs. 6B and 7B) by the pXRF instrument can be explained also by the Compton normalization method used in this equipment. It works well with samples containing up to 2–3% of the element analysed (Olympus, 2010; US EPA, 2007). The NIST materials have K contents of between 2 and 2.5%, while 75% of our samples show K concentrations of >2.4 wt.% and half of all our samples show >3.54 wt.% according to the ICP-MS/AE analysis (Table 1).

Since uranium is the element primarily responsible for generating radiogenic heat, and pXRF results for uranium show the greatest differences between the methods compared, radiogenic heat values (A_xrf) also display the highest deviation from analogous results based on γ-ray spectrometry and instrumental chemistry. In contrast to our results, Knight et al. (2021) reported underestimation of Th in pXRF results for low concentrations (<30 ppm), though this finding was based on only 15 measurements.

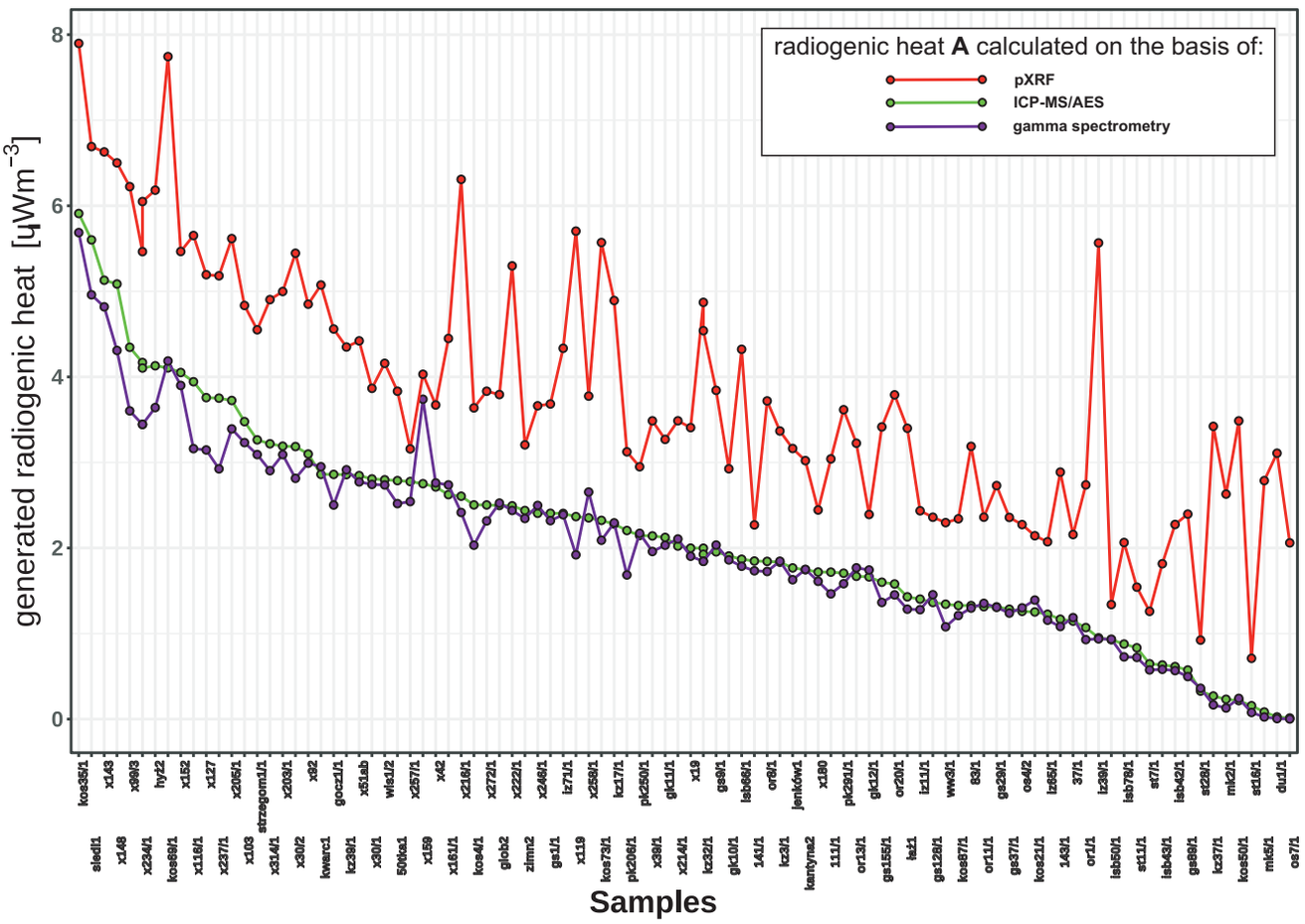

Fig. 10. The values of rock-generated radiogenic heat calculated on the basis of the three sets of K, U, Th concentrations from pXRF, ICP-MS/AES and gamma spectrometry analysis of the same samples

The samples are sorted and plotted in decreasing order according to the A values obtained from instrumental chemistry data (ICP-MS/AES)

The evaluation of the γ-ray spectrometry results show they differ from the pXRF measurements. For the Th_gamma results, there is a very good agreement with the chemistry results. Only a few samples with very low Th concentrations show enough underestimation, compared to the chemical analysis, to impact the calculated A_gamma value (Figs. 6E, 8B and 11D).

For the U_gamma data, although many more samples show underestimation compared to the chemistry results (Figs. 6C and 8A), the scale of this underestimation is so small that it does not significantly affect the calculated A_gamma values. Only a few samples, where U concentration is ~0 ppm in γ-ray spectrometry, display significantly lower values of calculated radiogenic heat (Fig. 11C). This finding is consistent with the study of Zhu et al. (2017), which also reported good agreement between gamma spectrometry and ICP-MS techniques and suggested that the datasets obtained by these two techniques can be combined for radiogenic heat calculations. Tuovinen et al. (2015) also reported acceptable agreement between gamma spectrometry and ICP-MS, though pointed to an underestimation of U and overestimation of Th by gamma spectrometry.

We have shown that the differences in calculated rock radiogenic heat values, especially for samples poor in uranium and thorium, stem from the varying ability of pXRF, and to a much lesser extent, γ-ray spectrometry, to measure concentrations of these elements. Many authors suggest that method performance and detection limits depend not only on instrument and preparation technique, but also on sample matrix composition (Tuovinen et al., 2015; Steiner et al., 2017; Lemière, 2018). The lack of full consistency in published comparative studies and in our own results regarding which method over- or underestimates elemental content also supports this conclusion. It is necessary to accept the challenges of measuring samples with low U and Th content, and there the potential exists for quality improvement. A set of local standards obtained by a reliable method is often advised for constructing a custom calibration (Durance et al., 2014; Steiner et al., 2017).

Knowledge of rock-generated radiogenic heat distribution is crucial for characterizing the heat and thermal state of a given region, as well as for proper evaluation of its geothermal potential (Hasterok and Chapman, 2011; Zhang et al., 2024; Rafiq et al., 2025). This heat, primarily generated by the radioactive de-

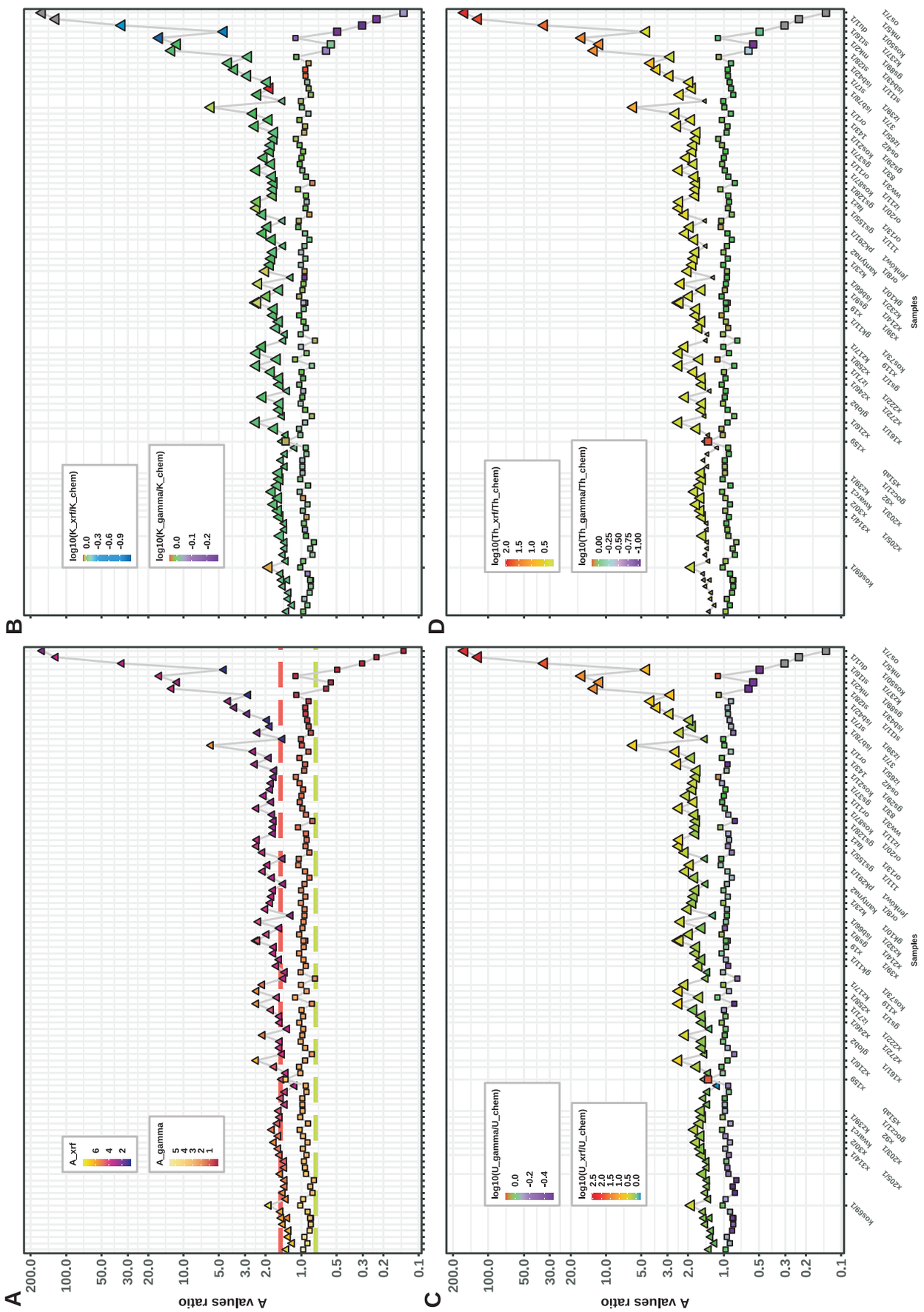

Fig. 11. The points on each panel are sorted from left to right according to decreasing values of radiogenic heat calculated from the chemical results (A_chem); triangles represent the ratio of pXRF-based results to chemistry-based results, while squares represent the gamma-based to chemistry-based results ratios

The points are colour-coded, accordingly to the legend inset of each panel: **A** – values of calculated radiogenic heat from pXRF and gamma spectrometry measurements, points below the green line show values lower than the corresponding A_chem measurements by 25% or more, while points above the red line show results higher by 50% or more. These samples are marked with larger symbols on panels **B**, **C** and **D**; (**B**, **C** and **D**) the decimal logarithms of the K, U and Th content ratios, from the measurements of pXRF and gamma respectively, to the concentrations of these elements obtained from the measurements of instrumental chemistry. Grey colour of points means that the pXRF or gamma spectrometry results were equal to 0. The y-axis has a decimal logarithmic scale

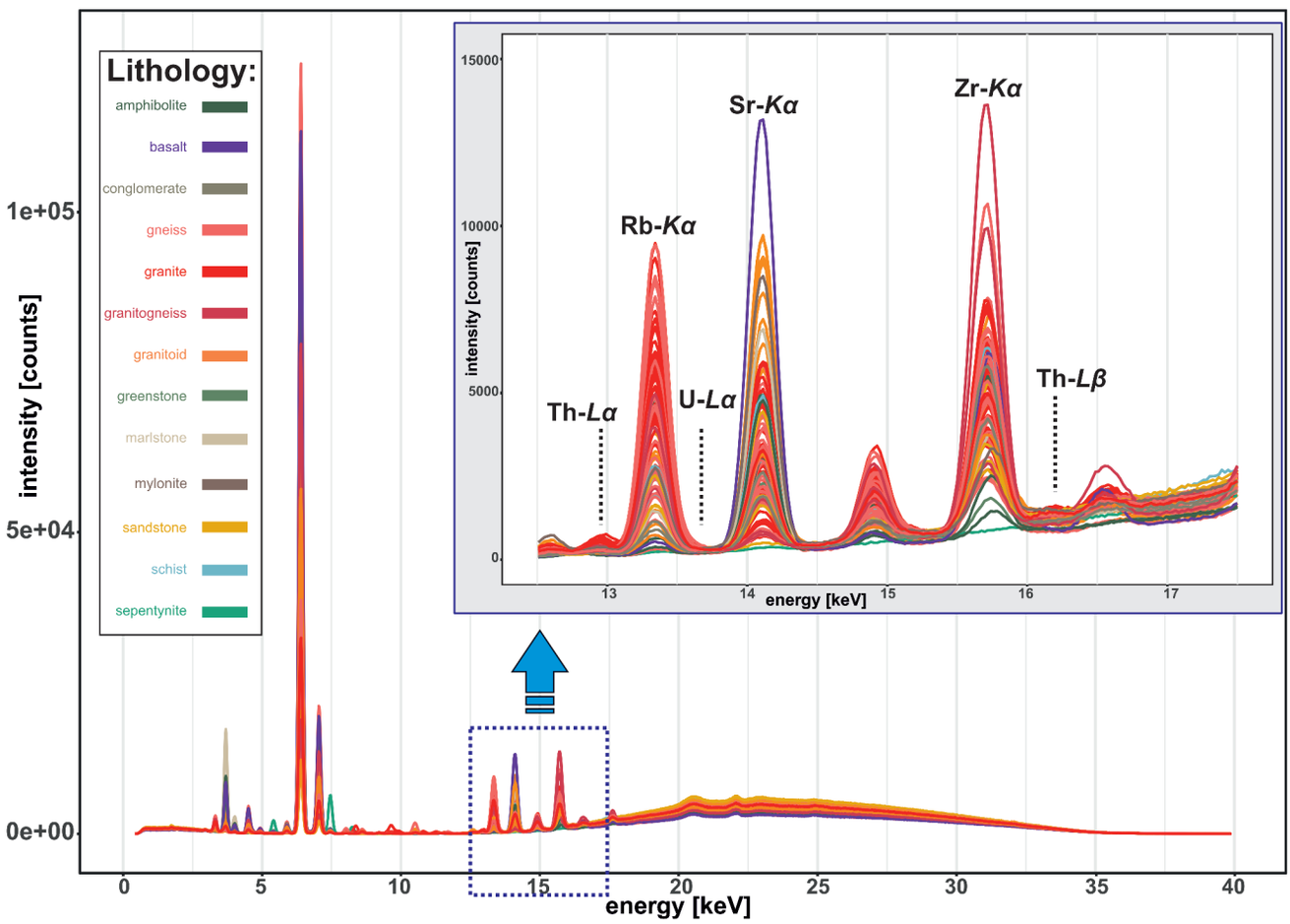

Fig. 12. Spectra (beam #1) obtained by the pXRF instrument

Visible K-lines from Rb, Sr and Zr peaks have significantly higher intensities than the Th and U L-lines

cay of isotopes of K, U and Th, represents an essential internal heat source that significantly influences the geothermal gradient and the thermal regime of the upper continental crust (Jaupart and Mareschal, 2007).

The contribution of this parameter becomes particularly significant in regions characterized by thick, acidic continental crust, especially those hosting large granitoid intrusions or metamorphic complexes, which serve as natural accumulators of heat-producing elements (Rudnick and Fountain, 1995). For instance, Zhang et al. (2024) reported that radiogenic heat production contributed 39–70°C to the formation of hot dry rock (HDR) resources in the northeastern Gonghe basin. The high concentration of these isotopes within granitic plutons often leads to the formation of so-called High Heat Flow Provinces, where crustal radiogenic heat production can significantly account for the total surface heat flow (Roy et al., 1968; Lachenbruch, 1971; Mareschal and Jaupart, 2013).

Taking into account the complex geological structure of the Sudetes, also including the presence of granite plutons, the correct estimation of the amount of radiogenic heat produced by the rocks is particularly important for geothermal prospecting in this region (Dowgiałło, 2002; Puziewicz et al., 2012; Majorowicz, 2021).

CONCLUSIONS

Portable XRF measurements may significantly overestimate the concentrations of U and Th, especially for samples having <10 ppm of these elements. Gamma spectrometry, by comparison, can slightly underestimate concentrations of these elements compared to ICP-MS/AES data. Each of these techniques has its advantages and disadvantages for analysing K, U and Th contents under laboratory conditions. Instrumental chemical analysis can provide the most accurate results, even for samples with minimal amounts of U and Th. However, it is expensive and requires the most complex sample pre-treatment. The two other methods can be used as alternatives, but with some limitations. γ-spectrometry requires a relatively large amount of material for analysis. Nevertheless, if sample preparation and instrument setup are correct, its consistency with instrumental chemistry is more than sufficient. Portable pXRF, although primarily a field screening tool, can also be used for a large number of laboratory measurements when a small amount of material is available and can be properly ground and homogenized.

We consider that our approach, based on robust sample preparation and statistical analysis, is appropriate for pXRF and gamma spectrometry measurements of U and Th for the most common lithologies in the Sudetes Mountains area. We plan to conduct further analyses on a larger set of samples, to achieve correction factors (from the regression lines), which may be used to correct pXRF measurements of U and Th. Such a set of corrections, especially for uranium measurements, will be helpful for rapid calculation of radiogenic heat values and for assessing the geothermal potential of the region.

Acknowledgements. This research was funded by the Polish National Fund for Environmental Protection and Water Management (agreement 579/2021/Wn-07/FG-go-dn/D).

REFERENCES

Aghdam, M.M., Kavanagh, M., Crowley, Q., 2024. Utilization of radiometric data for mapping primary and secondary sources of gamma radiation and radon/thoron release potentials in Ireland. Frontiers in Public Health, **12**,1443332; https://doi.org/10.3389/fpubh.2024.1443332

Altman, D.G., Bland, J.M., 1983. Measurement in medicine: the analysis of method comparison studies. The Statistician, **32**: 307–317; https://doi.org/10.2307/2987937

Anscombe, F.J., 1973. Graphs in statistical analysis. The American Statistician, **27**, 17–21; https://doi.org/10.1080/00031305.1973.10478966

Bablok, W., **Passing, H.**, **Bender, R.**, **Schneider, B.**, **1988.** A general regression procedure for method transformation. Application of Linear Regression Procedures for Method Comparison Studies in Clinical Chemistry, Part III. Journal of Clinical Chemistry and Laboratory Medicine, **26**: 783–790; http://doi/org/10.1515/cclm.1988.26.11.783

Beardsmore, G.R., **Cull, J.P., 2001.** Crustal Heat Flow: a Guide to Measurement and Modelling. Cambridge University Press, Cambridge.

Birch, F., **Roy, R.F.**, **Decker, E.R., 1968**. Heat flow and thermal history in New England and New York. Studies of Appalachian Geology Northern Maritime: 437–451; https://cir.nii.ac.jp/crid/1571135649246612224

Dowgiałło, J., 2002. The Sudetic geothermal region of Poland. Geothermics, **31**: 343–359.

Durance, P., **Jowitt, S.M.**, **Bush, K., 2014**. An assessment of portable X-ray fluorescence spectroscopy in mineral exploration, Kurnalpi Terrane, Eastern Goldfields Superterrane, Western Australia. Applied Earth Science, **123**: 150–163; https://doi.org/10.1179/1743275814Y.000000005

Fall, M., **Baratoux, D.**, **Jessell, M.**, **Ndiaye, P.M.**, **Vanderhaeghe, O.**, **Moyen, J.F.**, **Baratoux, L., Bonzi, W.M.-E.**, **2020**. The redistribution of thorium, uranium, potassium by magmatic and hydrothermal processes versus surface processes in the Saraya Batholith (Eastern Senegal): insights from airborne radiometrics data and topographic roughness. Journal of Geochemical Exploration, **219**, 106633; https://doi.org/10.1016/j.gexplo.2020.106633

Foote, R.S., **Frick, N.E.**, **2001**. Time variations of natural gamma radiation. Environmental. Geosciences, **8**: 130–139; https://doi.org/10.1046/j.1526-0984.2001.82005.x

Giavarina, D., **2015**. Understanding Bland Altman analysis. Biochemia Medica, **25**: 141–151; https://doi.org/10.11613/BM.2015.015

Haenel, R., **Rybach, L.**, **Stegena, L.**, **1988**. Handbook of Terrestrial Heat-Flow Density Determination. Springer Netherlands, Dordrecht.

Hanson, B., **2025**. ChemoSpec: Exploratory Chemometrics for Spectroscopy_. R package version 6.3.1; https://CRAN.R-project.org/package=ChemoSpec

Hasterok, D., Chapman, D.S., 2011. Heat production and geotherms for the continental lithosphere. Earth and Planetary Science Letters, **307**: 59–70; https://doi.org/10.1016/j.epsl.2011.04.034

Hasterok, D., **Webb, J.**, **2017.** On the radiogenic heat production of igneous rocks. Geoscience Frontiers, **8**: 919–940; https://doi.org/10.1016/j.gsf.2017.03.006

James, G., **Witten, D.**, **Hastie, T.**, **Tibshirani, R.**, **Taylor, J.E.**, **2023**. An introduction to statistical learning: with applications in Python. Springer, Cham, Switzerland.

Jaupart, C., **Mareschal, J.C., 2007**. Heat flow and thermal structure of the lithosphere. In: Treatise on Geophysics, vol. 6. Elsevier Science and Technology.

Jaupart, C., **Mareschal, J. C.**, **Iarotsky, L.**, **2016**. Radiogenic heat production in the continental crust. Lithos, **262**: 398–427; https://doi.org/10.1016/j.lithos.2016.07.017

Kalita, S., **Jodlowski, P.**, **Niewodniczański, J.**, **1996**. Time factor on sealed sample storage in 226Ra determination by its daughters decay. In: Proceedings of International Conference Technologically Enhanced Natural Radiation Caused by Non-Uranium Mining: 251–255.

Knight, R.D., **Kjarsgaard, B.A.**, **Potter, E.G.**, **Plourde, A., 2021**. Uranium, thorium, and potassium analyses using pXRF spectrometry; https://ostrnrcan-dostrncan.canada.ca/handle/1845/269407

Kozlovska, M., **Sybkova, H.**, **Otahal, P.P.**, **2023**. Radiation monitoring after experimental dirty bomb explosion. Radiation Protection Dosimetry, **199**: 1012–1020; https://doi.org/10.1093/rpd/ncad105

Kuila, U., **McCarty, D.K.**, **Derkowski, A.**, **Fischer, T.B.**, **Prasad, M.**, **2014**. Total porosity measurement in gas shales by the water immersion porosimetry (WIP) method. Fuel, **117**: 1115–1129; https://doi.org/10.1016/j.fuel.2013.09.073

Lachenbruch, A.H.,**1970**. Crustal temperature and heat production: Implications of the linear heat-flow relation. Journal of Geophysical Research, **75**: 3291–3300.

Lachenbruch, A.H.,**1971**. Vertical gradients of heat production in the continental crust 1. Theoretical detectability from near-surface measurements. Journal of Geophysical Research, **76**: 3842–3851; https://doi.org/10.1029/JB076i017p03842

Lemière, B., **2018**. A review of pXRF (field portable X-ray fluorescence) applications for applied geochemistry. Journal of Geochemical Exploration, **188**: 350–363; https://doi.org/10.1016/j.gexplo.2018.02.006

Lis, J., **Pasieczna, A.**, **Strzelecki, R.**, **Wołkowicz, S.**, **Lewandowski, P., 1997**. Geochemical and radioactivity mapping in Poland. Journal of Geochemical Exploration, **60**: 39–53; https://doi.org/10.1016/S0375-6742(97)00024-1

Ludbrook, J., **2010**. Linear regression analysis for comparing two measurers or methods of measurement: but which regression? Clinical and Experimental Pharmacology and Physiology, **37**: 692–699; https://doi.org/10.1111/j.1440-1681.2010.05376.x

Majorowicz, J., **2021**. Review of the heat flow mapping in Polish sedimentary basin across different tectonic terrains. Energies, **14**, 6103; https://doi.org/10.3390/en14196103

Mareschal, J.C., **Jaupart, C.**, **2013**. Radiogenic heat production, thermal regime and evolution of continental crust. Tectonophysics, **609**: 524–534; https://doi.org/10.1016/j.tecto.2012.12.001

Melquiades, F.L., Bastos, R.O., Rampim, L., Sandrino, I.I., Rodriguez, D.G., Parreira, P.S., 2024. Thorium and uranium rapid quantification in soil with portable X-ray fluorescence. Soil Science Society American Journal, **88**: 557–564; https://doi.org/10.10002/saj2.20639

Mazur, S., Aleksandrowski, P., Gągała, Ł., 2025. The Geology of Variscan Sudetes and their northern foreland. In: The Variscan Orogen of Central Europe (ed. U. Linnemann): 429–476. Springer Nature Switzerland, Cham.

McCay, A.T., **Harley, T.L.**, **Younger, P.L.**, **Sanderson, D.C.W.**, **Cresswell, A.J.**, **2014**. Gamma-ray spectrometry in geothermal exploration: state of the art techniques. Energies, **7**: 4757–4780; https://doi.org/10.3390/en7084757

Moskalewicz, D., 2022. Handheld gammma-ray spectrometry at geological exposures – methods and applications (in Polish with English summary). Przegląd Geologiczny, **70**: 806–815; https://doi.org/10.7306/2022.31

Nisi, S., **Di Vacri, A.**, **Di Vacri, M.L.**, **Stramenga, A.**, **Laubenstein, M., 2009**. Comparison of inductively coupled mass spectrometry and ultra low-level gamma-ray spectroscopy for ultra low background material selection. Applied Radiation and Isotopes, **67**: 828–832; https://doi.org/10.1016/j.apradiso.2009.01.021

NIST, **2005**. Standard Reference Materials – Historical Archived Certificates.

Olympus, **2010**. DELTA Family Handheld XRF Analyzer User Manual.

Passing, H., **Bablok, W.**, **1983**. A new biometrical procedure for testing the equality of measurements from two different analytical methods. Application of linear regression procedures for method comparison studies in Clinical Chemistry, Part I. Journal of Clinical Chemistry and Laboratory Medicine, **21**: 709–720; https://doi.org/10.1515/cclm.1983.21.11.709

Passing, H., **Bablok, W.**, **1984**. Comparison of several regression procedures for method comparison studies and determination of sample sizes application of linear regression procedures for method comparison studies in Clinical Chemistry, Part II. Journal of Clinical Chemistry and Laboratory Medicine, **22**: 431–445; https://doi.org/10.1515/cclm.1984.22.6.431

Potapov, S., Model, F., Schuetzenmeister, A., Manuilova, E., Dufey, F., Raymaekers, J., 2012. mcr: Method Comparison Regression. 1.3.3.1; https//doi.org/10.32614/CRAN.package.mcr

Puziewicz, J., **Czechowski, L.**, **Krysiński, L.**, **Majorowicz, J.**, **Matusiak-Małek, M.**, **Wróblewska, M.**, **2012**. Lithosphere thermal structure at the eastern margin of the Bohemian Massif: a case petrological and geophysical study of the Niedźwiedź amphibolite massif (SW Poland). International Journal of Earth Science, **101**: 1211–1228; https://doi.org/10.1007/s00531-011-0714-7

Rafiq, J., Abu-Mahfouz, I.S., Whattam, S., 2025. Petrogenesis, radiogenic heat production, and geothermal potential of host rocks in the Al-Lith geothermal system, Western Saudi Arabia. Renewable Energy, **250**, 123362; https://doi.org/10.1016/j.renene.2025.123362

Roy, R.F., **Blackwell, D.D.**, **Birch, F., 1968**. Heat generation of plutonic rocks and continental heat flow provinces. Earth and Planetary Science Letters, **5**: 1–12.

Rudnick, R.L., **Fountain, D., 1995.** Nature and composition of the continental crust: a lower crustal perspective. Reviews of Geophysics, **33:** 267–309; https://doi.org/10.1029/95RG01302

Rybach, L., **1988**. Determination of the Heat Production Rate. In: Handbook of Terrestrial Heat-Flow Density Determination, 125–142; https://doi.org/10.1007/BF00878955

Sanjurjo-Sánchez, J., **Barrientos Rodríguez, V.**, **Arce Chamorro, C.**, **Alves, C.**, **2022**. Estimating the Radioactive Heat Production of a Granitic Rock in the University of A Coruña (Galicia, Northwest Spain) by Gamma-ray Spectrometry. Applied Sciences, **12**, 11965; https://doi.org/10.3390/app122311965

Schön, J., **2015**. Physical properties of rocks: fundamentals and principles of petrophysics, 2nd edition. Elsevier, Amsterdam, Netherlands.

Sliaupa, S., **Motuza, G.**, **Karabliova, L.**, **Motuza, V.**, **Zaludiene, G.**, **2005.** Hot granites of southwest western Lithuania: new geo-thermal prospects. Technika Poszukiwań Geologicznych, **3**: 26–34.

Solecki, A., **Śliwiński, W.**, **Wojciechowska, I.**, **Tchorz-Trzeciakiewicz, D.**, **Syryczyński, P.**, **Sadowska, M.**, **Makowski, B.**, **2011**. Ocena możliwości występowania mineralizacji uranowej w Polsce na podstawie wyników prac geologiczno-poszukiwawczych (in Polish). Przegląd Geologiczny, **59**: 98–110.

Steiner, A.E., **Conrey, R.M.**, **Wolff, J.A.**, **2017**. PXRF calibrations for volcanic rocks and the application of in-field analysis to the geosciences. Chemical Geology, **453**: 35–54; https://doi.org/10.1016/j.chemgeo.2017.01.023

Strzelecki, R., **Wołkowicz, S.**, **2019**. History of Uranium research in the Polish Geological Institute (in Polish with English summary). Przegląd Geologiczny, **67**: 75–90.

Strzelecki, R., **Wołkowicz, S.**, **Szewczyk, J.**, **Lewandowski, P.**, **1994**. Mapy radioekologiczne Polski Część II: Mapy koncentracji uranu, toru i potasu w Polsce (in Polish).

Tuovinen, H., **Vesterbacka, D.**, **Pohjolainen, E.**, **Read, D.**, **Solatie, D.**, **Lehto, J.**, **2015**. A comparison of analytical methods for determining uranium and thorium in ores and mill tailings. Journal of Geochemical Exploration, **148**: 174–180; https://doi.org/10.1016/j.gexplo.2014.09.004

US EPA, **2007**; https://www.epa.gov/sites/default/files/2015-12/documents/6200.pdf

Wedepohl, **K.H., 1995**. The composition of the continental crust. Geochimica et Cosmochimica Acta, **59**: 1217–1232; https://doi.org/10.1016/0016-7037(95)00038-2

Wickham, H., 2016. Data analysis. In: ggplot2. Springer International Publishing, Cham.

Wollenberg, H.A., **Smith, A.R.**, **1987**. Radiogenic heat production of crustal rocks: An assessment based on geochemical data. Geophysical Research Letters, **14**: 295–298; https://doi.org/10.1029/GL014i003p00295

Van Grieken, R., **Markowicz, A.**, **2001**. Handbook of X-ray Spectrometry, 2nd edn. CRC Press.

Zhang, L., **Li, X.**, **Zhang, S.**, **Zhu, G.**, **Xu, W.**, **Feng, Q.**, **Deng, Z.**, **2024**. Deep-seated radiogenic heat production characteristics in the northeastern Gonghe basin (northeastern Qinghai-Tibet plateau) from deep borehole samples: Implications for the formation of hot dry rock resources. Geothermics, **123**, 103110.

Zhou, S., **Wang, J.**, **Wang, W.**, **Liao, S.**, **2023**. Evaluation of portable X-ray fluorescence analysis and its applicability as a tool in geochemical exploration. Minerals, **13**, 166; https://doi.org/10.3390/min13020166

Zhu, C., **Xu, M.**, **Qiu, N.**, **Hu, S.**, **2017**. Comparison of γ-ray spectrometry and ICP-MS methods for measuring radioactive heat-producing elements of rocks: a case study on borehole samples from the Sichuan Basin, China. Journal of Radioanalytical and Nuclear Chemistry, **314**: 1527–1537; https://doi.org/10.1007/s10967-017-5576-4

APPENDIX 1

Sample	K_chem [wt.%]	U_chem [ppm]	Th_chem [ppm]	K_gamma [wt.%]	U_gamma [ppm]	Th_gamma [ppm]	K_xrf [wt.%]	U_xrf [ppm]	Th_xrf [ppm]	A_chem [uW/m^3]	A_gamma [uW/m^3]	A_xrf [uW/m^3]	BD [g/cm^3]	ROCK_TYPE	LITHLOGY	GEOLOGICAL UNIT
111/1	2.45	2.51	11.9	2.37	2.03	10.23	2.44	3.97	25	1.72	1.46	3.04	2.78	light-coloured metamorphic	gneiss	Góry Sowie Gneiss Massif
gs29/1	1.88	2.14	9.22	1.9	2.15	9.08	1.79	4.33	22	1.31	1.31	2.73	2.64	light-coloured metamorphic	gneiss	Góry Sowie Gneiss Massif
x314/1	3.38	4.76	27.7	3.58	3.49	27.43	3.17	7.37	44	3.22	2.9	4.9	2.54	acidic igneous	granite	Izera-Karkonosze Massif
gk10/1	4.07	2.86	14.05	4.18	2.03	16.36	3.6	3.7	27.13	1.91	1.86	2.93	2.53	acidic igneous	granitoid	Kudowa Granite Pluton
gs155/1	2.66	3.95	5.75	2.84	2.91	6	2.33	8.17	17.07	1.6	1.36	3.42	2.64	light-coloured metamorphic	gneiss	Góry Sowie Gneiss Massif
kz17/1	3.35	4.22	13.15	3.05	4.5	12.64	3.32	10	29	2.28	2.29	4.89	2.71	acidic igneous	granitoid	Kłodzko-Złoty Stok Granite Pluton
kz3/1	3.05	3.31	11.1	2.81	3.52	10.74	2.85	4.97	27.67	1.83	1.85	3.37	2.65	acidic igneous	granitoid	Kłodzko-Złoty Stok Granite Pluton
kz32/1	3.09	3.4	12.15	2.77	3.43	10.23	3.35	9	31.67	2	1.84	4.87	2.74	acidic igneous	granitoid	Kłodzko-Złoty Stok Granite Pluton
kz32/1*	3.08	3.4	11.15	2.77	3.43	10.23	3.3	9	27	1.93	1.84	4.54	2.74	acidic igneous	granitoid	Kłodzko-Złoty Stok Granite Pluton
kz37/1	1.01	0.38	1.06	0.88	0.21	0.45	0.91	7.17	18	0.27	0.17	3.42	2.9	dark-coloured metamorphic	amphibolite	Kłodzko Metamorphic Massif
kz39/1	3.51	3.91	24.2	3.42	4.28	23.75	3.52	5.83	39.33	2.86	2.91	4.35	2.6	acidic igneous	granitoid	Kłodzko-Złoty Stok Granite Pluton
du1/1	0.1	0.03	0.13	0.07	0	0	0	8.57	8.8	0.03	0.01	3.11	2.95	dark-coloured metamorphic	greenstone	Kaczawa greenstoneand-slate fold belt
gk12/1	2.13	2.65	12.85	2.23	2.56	14.31	1.75	2.5	24.93	1.66	1.74	2.39	2.57	acidic igneous	granitoid	Kudowa Granite Pluton
os7/1	0.02	0.03	0.06	0.02	0	0	0	6.03	6.37	0.01	0	2.06	2.76	dark-coloured metamorphic	sepentynite	Ślęża Massif
143/1	1.59	0.99	11.05	1.66	0.55	11.44	1.54	3.87	24.67	1.17	1.08	2.89	2.75	light-coloured metamorphic	gneiss	Góry Sowie Gneiss Massif
gk11/1	3.67	4.12	12.45	3.7	3.31	14.09	3.16	5.67	24.53	2.12	2.03	3.27	2.58	acidic igneous	granitoid	Kudowa Granite Pluton
glob2	4.16	4.37	16.75	3.86	4.09	18.57	3.56	6.23	30.1	2.5	2.52	3.79	2.57	acidic igneous	granite	Strzegom-Sobótka Granite Pluton
gocz1/1	3.97	4.86	20.3	3.86	3.76	19.17	3.37	8.57	32.6	2.86	2.5	4.56	2.59	acidic igneous	granite	Strzegom-Sobótka Granite Pluton
kantyna2	3.25	2.59	13.3	2.95	2.41	14.39	2.74	4.37	26.7	1.75	1.75	3.02	2.55	acidic igneous	granite	Strzegom-Sobótka Granite Pluton
kwarc1	4.01	5.12	18.95	3.74	5.34	19.76	3.62	9.93	34.33	2.86	2.95	5.07	2.61	acidic igneous	granite	Strzegom-Sobótka Granite Pluton
siedl1	4.3	15.35	21	4.1	12.9	20.85	3.63	16.1	35.23	5.6	4.96	6.69	2.61	acidic igneous	granite	Strzegom-Sobótka Granite Pluton
strzegom1/1	3.59	6.05	21.4	3.49	5.66	20.45	3.16	7.07	37.07	3.26	3.09	4.55	2.64	acidic igneous	granite	Strzegom-Sobótka Granite Pluton
zimn2	3.94	2.77	22	3.58	2.6	21.65	3.3	2.5	35.37	2.44	2.34	3.21	2.58	acidic igneous	granite	Strzegom-Sobótka Granite Pluton
37/1	2.25	1.57	8.88	2.29	1.61	9.29	2.2	2.5	20.73	1.15	1.19	2.16	2.58	light-coloured metamorphic	gneiss	Góry Sowie Gneiss Massif
50tka1	4.04	4.54	19.85	3.85	4.12	17.66	3.57	5.17	33.6	2.79	2.52	3.83	2.62	acidic igneous	granite	Strzegom-Sobótka Granite Pluton
hyż2	4.17	9.56	21	3.61	8.07	19.96	3.68	14.17	34.87	4.13	3.64	6.18	2.61	acidic igneous	granite	Strzegom-Sobótka Granite Pluton
wis1/2	4.05	4.34	20.9	3.68	4.35	20.37	3.56	5.73	36.57	2.8	2.74	4.16	2.61	acidic igneous	granite	Strzegom-Sobótka Granite Pluton
x143	4.36	9.11	40.5	4	7.27	43.03	3.56	10.1	61	5.13	4.82	6.63	2.51	acidic igneous	granite	Izera-Karkonosze Massif
x148	4.16	9.93	35.1	3.93	6.61	36.09	3.43	11.63	51	5.09	4.31	6.5	2.57	acidic igneous	granite	Izera-Karkonosze Massif
x237/1	3.89	7.89	24.2	3.8	3.9	26.51	3.32	9.17	42.27	3.75	2.93	5.18	2.51	acidic igneous	granite	Izera-Karkonosze Massif
x30/1	4.02	4.8	19.35	3.77	4.06	21.46	3.68	5.63	32.43	2.81	2.74	3.87	2.61	acidic igneous	granite	Izera-Karkonosze Massif
x257/1	3.78	4.34	20.9	3.65	3.21	21.82	3.39	2.5	34	2.78	2.54	3.16	2.61	acidic igneous	granite	Izera-Karkonosze Massif
x161/1	3.54	5.26	15.4	3.38	5.07	18.01	3.18	9	29	2.62	2.74	4.45	2.61	acidic igneous	granite	Izera-Karkonosze Massif
x205/1	4.08	6.3	29.8	4.07	4.55	31.24	3.48	9.7	47.2	3.72	3.39	5.62	2.5	acidic igneous	granite	Izera-Karkonosze Massif
141/1	3	2.86	12.75	2.44	2.81	11.91	2.81	2.5	20.47	1.85	1.73	2.27	2.68	light-coloured metamorphic	gneiss	Góry Sowie Gneiss Massif
x246/1	3.6	3.77	18.4	3.49	4.02	18.97	3.3	4.97	33.4	2.41	2.5	3.66	2.56	acidic igneous	granite	Izera-Karkonosze Massif
łaż1	3.74	1.74	9.29	3.46	1.44	8.72	3.82	6.17	20.17	1.43	1.29	3.4	2.78	acidic igneous	granite	Strzegom-Sobótka Granite Pluton
x19	3.12	3.39	13.7	3.01	3.08	13.59	2.85	5.5	27.2	2	1.9	3.41	2.6	acidic igneous	granite	Strzegom-Sobótka Granite Pluton
x92	3.7	5.38	24.9	3.96	4.02	28.03	3.26	8.2	42.67	3.1	2.99	4.85	2.45	acidic igneous	granite	Izera-Karkonosze Massif
x180	3.92	3.21	10	3.75	2.74	10.31	3.33	3.7	20	1.72	1.61	2.44	2.53	acidic igneous	granite	Izera-Karkonosze Massif
x272/1	3.12	3.37	21.5	3.15	2.69	21.22	2.85	4.83	36.33	2.5	2.32	3.83	2.59	acidic igneous	granite	Izera-Karkonosze Massif
x30/2	4.06	5.11	23.8	3.84	4	22.68	3.61	9.47	41.67	3.19	2.81	5.45	2.61	acidic igneous	granite	Izera-Karkonosze Massif
x203/1	3.79	5.89	21.4	3.64	4.8	24.22	3.38	8.5	39.17	3.19	3.09	5	2.6	acidic igneous	granite	Izera-Karkonosze Massif
x214/1	3.62	3.48	14.25	3.61	3.04	17.22	3.27	5.93	28.17	2.02	2.11	3.49	2.51	acidic igneous	granite	Izera-Karkonosze Massif
x216/1	3.62	3.54	22.3	3.39	3.47	19.92	3.16	14.53	37.8	2.61	2.42	6.31	2.56	acidic igneous	granite	Izera-Karkonosze Massif
83/1	1.72	1.98	9.37	1.64	1.88	9.43	1.71	5.27	23.3	1.33	1.3	3.19	2.76	light-coloured metamorphic	gneiss	Góry Sowie Gneiss Massif
x222/1	3.53	3.89	18.35	3.49	3.81	17.88	3.2	10.43	35.67	2.49	2.44	5.3	2.63	acidic igneous	granite	Izera-Karkonosze Massif
x234/1	3.84	9.09	23.7	3.75	6.05	25.26	3.24	12.73	40.2	4.1	3.44	6.05	2.57	acidic igneous	granite	Izera-Karkonosze Massif
x234/1*	3.83	9.46	23.3	3.75	6.05	25.26	3.23	11.07	37.6	4.17	3.44	5.46	2.57	acidic igneous	granite	Izera-Karkonosze Massif
pk206/1	1.06	7.72	4.08	1.11	5.58	3.99	0.91	10.37	8.63	2.2	1.68	3.12	2.5	light-coloured metamorphic	schist	Niemcza Shear Zone
pk250/1	3.61	2.43	21.1	3.48	2.04	23.14	3.02	2.5	34.37	2.15	2.17	2.95	2.44	acidic igneous	granitoid	Strzelin Gneiss-and-Granite Massif
x258/1	3.42	3.1	19.9	3.51	2.87	25.22	3.06	5.43	32.97	2.35	2.65	3.78	2.59	acidic igneous	granite	Izera-Karkonosze Massif
x51ab	4.49	4.96	19.45	4.15	4.01	22.29	3.87	7.97	32.73	2.85	2.77	4.42	2.57	acidic igneous	granite	Izera-Karkonosze Massif
x99/3	3.7	8.93	28.4	3.54	6.4	26.79	3.11	12.9	42.73	4.35	3.6	6.22	2.56	acidic igneous	granite	Izera-Karkonosze Massif
x116/1	4.04	7.87	26.6	3.88	4.86	26.06	3.43	12.1	37.7	3.94	3.16	5.65	2.53	acidic igneous	granite	Izera-Karkonosze Massif
x119	3.55	3.72	20.3	3.35	2.21	19	3.01	14.27	35.17	2.37	1.92	5.7	2.41	acidic igneous	granite	Izera-Karkonosze Massif
gs89/1	1.58	1.18	2.29	1.66	0.97	1.83	1.42	5	15.1	0.57	0.5	2.4	2.63	acidic igneous	granitoid	Góry Sowie Gneiss Massif
x127	3.91	6.44	28.6	3.71	3.59	30.26	3.27	8.83	42.2	3.76	3.15	5.19	2.56	acidic igneous	granite	Izera-Karkonosze Massif
x103	3.93	6.02	26.3	3.5	4.59	28.42	3.39	8.27	39.3	3.48	3.23	4.83	2.54	acidic igneous	granite	Izera-Karkonosze Massif
x152	3.9	7.34	33	3.77	5.71	36.87	3.36	9.57	47.93	4.05	3.9	5.47	2.43	acidic igneous	granite	Izera-Karkonosze Massif
x159	3.78	5.44	16.85	3.96	7.28	24.62	3.39	7.17	30.13	2.75	3.74	4.03	2.58	acidic igneous	granite	Izera-Karkonosze Massif
x39/1	5.37	4.26	11.3	5.07	2.96	13.7	4.5	7.47	21.2	2.14	1.96	3.49	2.5	acidic igneous	granite	Izera-Karkonosze Massif
x42	3.54	5.23	16.7	3.39	4.61	19.91	3.13	5.8	29.3	2.71	2.76	3.67	2.62	acidic igneous	granite	Izera-Karkonosze Massif
kos87/1	3.98	1.71	9.23	3.94	1.33	8.94	3.51	3.5	18.4	1.33	1.21	2.34	2.57	light-coloured metamorphic	gneiss	Orlica-Śnieżnik Dome
kos96/1	2.95	1.81	11.25	2.87	1.63	11.1	3.29	5.3	25.43	n.a.	n.a.	n.a.	n.a.	light-coloured metamorphic	gneiss	Orlica-Śnieżnik Dome
jenków1	2.55	3.07	11.1	2.45	2.65	10.78	2.52	4.7	25.17	1.77	1.63	3.16	2.7	light-coloured metamorphic	schist	Kaczawa greenstoneand-slate fold belt
or20/1	2.51	2.66	10.5	2.46	2	11.18	2.64	7.3	25.53	1.58	1.45	3.79	2.64	light-coloured metamorphic	gneiss	Orlica-Śnieżnik Dome
gs1/1	3.3	5.56	11.55	3.31	5.29	11.27	3.08	8.17	21.23	2.41	2.32	3.68	2.59	light-coloured metamorphic	gneiss	Góry Sowie Gneiss Massif
kos35/1	4.08	20.7	8.09	4.01	19.59	8.94	3.55	26.67	16.73	5.91	5.69	7.9	2.54	light-coloured metamorphic	gneiss	Orlica-Śnieżnik Dome
kos21/1	3.79	1.87	7.55	3.9	2.3	7.89	3.44	3.4	15.6	1.25	1.39	2.14	2.59	light-coloured metamorphic	gneiss	Orlica-Śnieżnik Dome
kos4/1	3.81	7.82	6.74	3.93	5.71	6.94	3.33	11.37	12.27	2.5	2.03	3.64	2.41	light-coloured metamorphic	gneiss	Orlica-Śnieżnik Dome
kos69/1	4.53	5.03	34.2	4.42	5.11	35.18	5.09	12.33	57.67	4.11	4.19	7.74	2.75	light-coloured metamorphic	gneiss	Orlica-Śnieżnik Dome
or13/1	4.21	2.39	12	4.19	2.08	14.71	3.75	6.33	21.63	1.67	1.77	3.22	2.53	light-coloured metamorphic	gneiss	Orlica-Śnieżnik Dome
pk291/1	2.85	3.15	9.94	2.7	2.73	9.9	2.86	7.4	21.93	1.71	1.58	3.62	2.66	light-coloured metamorphic	schist	Kamieniec Ząbkowicki Metamorphic Fold Belt
st11/1	1	1.76	5.1	1.02	1.44	4.54	1.22	2.5	13	0.83	0.72	1.54	2.53	clastic	marlstone	Intra-Sudetic Synclinorium
st16/1	0.04	0.39	1.15	0.02	0.12	0.85	0.01	2.5	2.67	0.16	0.08	0.71	2.29	clastic	sandstone	Intra-Sudetic Synclinorium
st28/1	1.49	0.54	1.96	1.5	0.6	2.28	1.3	3	3.23	0.33	0.36	0.92	2.25	clastic	sandstone	Intra-Sudetic Synclinorium
st7/1	1.25	1.36	3.94	1.16	1.09	3.89	1.07	2.5	9.77	0.65	0.57	1.26	2.41	clastic	sandstone	Intra-Sudetic Synclinorium
gs37/1	2.86	2.3	7.85	2.89	2.25	7.29	2.81	4.43	16.33	1.28	1.24	2.36	2.54	light-coloured metamorphic	gneiss	Góry Sowie Gneiss Massif
kos50/1	0.31	0.44	0.81	0.26	0.59	0.62	0.02	7.6	16.67	0.22	0.24	3.49	3	dark-coloured metamorphic	amphibolite	Orlica-Śnieżnik Dome
kos73/1	3.45	4.77	13.25	3.38	3.83	13.37	3.01	15.5	22.4	2.32	2.09	5.57	2.58	light-coloured metamorphic	gneiss	Orlica-Śnieżnik Dome
mk2/1	0.8	0.45	0.5	0.76	0.22	0.04	0.76	6.47	9.9	0.23	0.13	2.63	2.92	dark-coloured metamorphic	amphibolite	Kłodzko Metamorphic Massif
or1/1	1.88	1.57	7.73	1.74	1.37	6.58	1.79	5.53	17.43	1.07	0.93	2.74	2.65	light-coloured metamorphic	gneiss	Orlica-Śnieżnik Dome
or11/1	5.35	1.3	8.95	5.37	1.29	9.54	4.88	3.5	17	1.31	1.35	2.36	2.58	light-coloured metamorphic	gneiss	Orlica-Śnieżnik Dome
or8/1	2.59	4.66	9.24	2.73	3.88	10.12	2.8	9.53	20.87	1.84	1.73	3.72	2.42	light-coloured metamorphic	gneiss	Orlica-Śnieżnik Dome
mk5/1	0.37	0.12	0.22	0.29	0	0	0.19	7.17	9.13	0.08	0.03	2.79	2.99	dark-coloured metamorphic	amphibolite	Kłodzko Metamorphic Massif
iz11/1	3.06	2.49	8.46	3.1	1.95	8.58	3.12	3.8	19.13	1.4	1.28	2.43	2.57	light-coloured metamorphic	gneiss	Izera-Karkonosze Massif
iz39/1	0.85	1.53	5.72	0.81	1.47	5.83	0.89	6.17	48.67	0.95	0.94	5.57	2.98	basic igneous	basalt	Izera-Karkonosze Massif
iz9/1	3.92	4.11	12	3.99	3.19	10.52	3.52	6.8	20.07	n.a.	n.a.	n.a.	n.a.	light-coloured metamorphic	gneiss	Izera-Karkonosze Massif
gs128/1	2.03	2.79	7.28	2.1	2.98	7.81	1.73	4.5	15.83	1.36	1.45	2.36	2.65	light-coloured metamorphic	gneiss	Góry Sowie Gneiss Massif
iz71/1	4.55	2.75	21.6	4.58	2.13	23.66	4.09	3.43	49.33	2.4	2.39	4.33	2.53	acidic igneous	granitogneiss	Izera-Karkonosze Massif
gs9/1	2.52	3.72	11.4	2.62	4.09	11.03	2.57	7.5	24.37	1.96	2.03	3.84	2.7	light-coloured metamorphic	gneiss	Góry Sowie Gneiss Massif
isb42/1	0.88	1.07	4.12	0.97	0.88	4.04	0.81	4.63	15.5	0.61	0.57	2.27	2.62	clastic	conglomerate	Intra-Sudetic Synclinorium
isb43/1	0.51	1.62	3.11	0.56	1.41	3.06	0.42	4.43	10.93	0.63	0.58	1.82	2.52	clastic	conglomerate	Intra-Sudetic Synclinorium
isb50/1	2.1	1.78	6.08	2.17	1.8	6.03	1.78	2.5	10.43	0.93	0.93	1.34	2.39	clastic	sandstone	Intra-Sudetic Synclinorium
isb66/1	4.07	2.92	13.7	4.13	2.59	13.57	4.31	7.13	36	1.87	1.79	4.32	2.49	acidic igneous	latite	Intra-Sudetic Synclinorium
isb78/1	1.15	1.91	5.42	1.18	1.41	4.9	1.13	4.17	15.77	0.88	0.73	2.06	2.46	clastic	conglomerate	Intra-Sudetic Synclinorium
iz65/1	4.33	2.38	5.06	4.57	2.12	4.69	3.71	4.73	9.93	1.23	1.16	2.07	2.53	acidic igneous	granitogneiss	Izera-Karkonosze Massif
os4/2	2.74	1.06	12.2	2.67	0.84	13.74	2.26	2.5	22.83	1.26	1.3	2.27	2.55	light-coloured metamorphic	mylonite	Ślęża Massif
ww3/1	2.17	2.25	9.87	2.35	1.17	9.65	2.12	3.73	19.1	1.34	1.08	2.3	2.52	light-coloured metamorphic	gneiss	Wądroże Wielkie Gneiss Massif

Samples marked with an asterisk (*) were measured twice using IC-MS/AES and pXRF for quality control purposes; n.a. - not analysed due to lack of material. A_xrf values marked by red color are more than 3 times higher than A_chem; A_xrf values and A_gamma values marked by orange color are from 1.3 to 3 times higher than A_chem.

APPENDIX 2

Passing - Bablock regression principles

In this regression method, the slopes $\mathbf{a_{ij}}$ of the lines connecting each pair of points X_iY_i and X_jY_j are calculated (Fig. A2.1A, equation [A2.1]). The final slope **a** of the fitted regression line is the median of the calculated slopes (equation [A2.2]). The y-interception coefficient **b** of the regression line is also the median of the coefficients $\mathbf{b_i}$ (equation [A2.3]), which are determined from the intersection of lines crossing each data point with the Y axis when X value is equal to 0. The entire family of these lines has the slope **a,** which was calculated in steps [1] and [2] (Fig. A2.1B).

$$a_{ij}=\frac{Y_i-Y_j}{X_i-X_i},\ 1 \le i < j \le n \quad [A2.1]$$

$$a = \text{median}\{a_{ij}, i = 1, \ldots, n\},\ 1 \le i < j \le n \quad [A2.2]$$

$$\hat{b}=\text{median}\{b_i, i=1, \ldots, n\} \quad [A2.3]$$

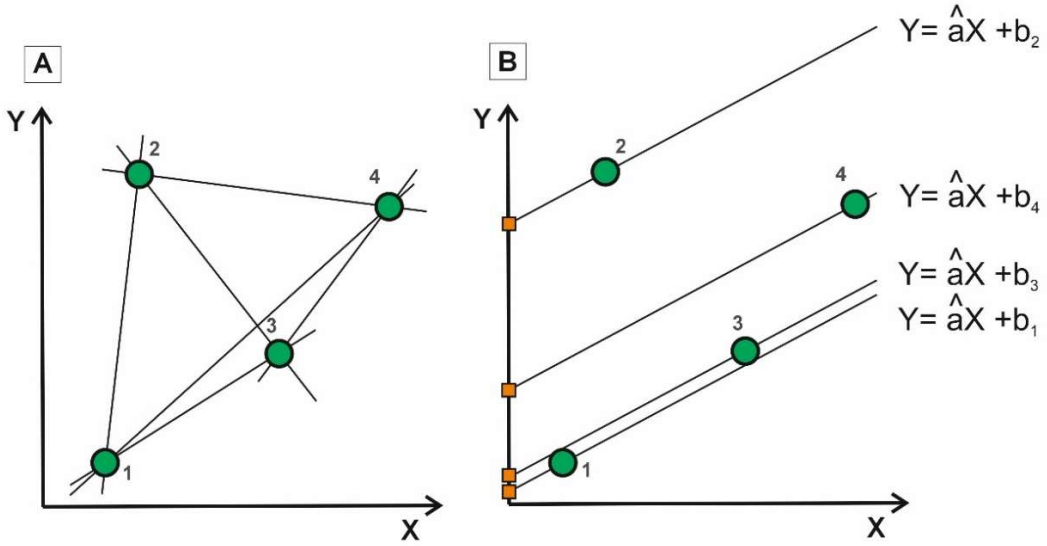

A2.1. Passing-Bablok regression principles presented in graphical from

Bland-Altman plots

On this type of plot, the coordinates of the points are not the direct measurement results. The x-axis displays the average value of the measurements obtained by both techniques for each i-th sample, denoted as M_i, and these values are arranged in an ascending order. The y-axis shows the relative difference values, denoted as D_i. This is calculated as the difference between the measurements from the two techniques for each i-th sample, divided by the Mi value, and then multiplied by 100% (Fig. A2.2). Additionally, the plots include two horizontal lines: a line at 0 to represent no difference between the methods and a line indicating mean percentage difference (MPD), which is an average of all M_i values.

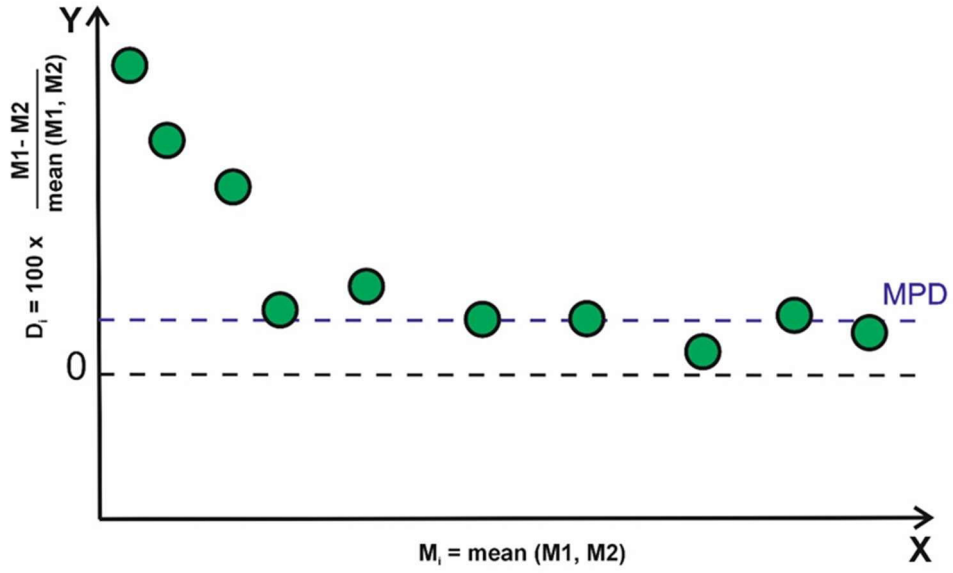

A2.2. Example of Bland-Altman plot. MPD – mean percent difference